Temperature and circulation in the stratospheres of the outer planets

Barney J. Conrath

Laboratory for Extraterrestrial Physics

NASA Goddard Space Flight Center, Code 693

Greenbelt MD 20771

Peter J. Gierasch

Astronomy Department, Space Sciences Building

Cornell University

Ithaca NY 14853

Stephen S. Leroy

Division of Geological and Planetary Sciences 170-25

California Institute of Technology

Pasadena CA 91125

January 1989

24 pages

13 figures

1 table

Abstract

A zonally symmetric, linear radiative-dynamical model is compared with observations of the upper tropospheres and stratospheres of the outer planets. Seasonal variation is included in the model. Friction is parameterized by linear drag (Rayleigh friction). Gas opacities are accounted for but aerosols are omitted. Horizontal temperature gradients are small on all the planets. Seasonal effects are strongest on Saturn and Neptune but are weak even in these cases, because the latitudinal gradient of radiative heating is weak. Seasonal effects on Uranus are extremely weak because the radiative time constant is longer than the orbital period. The one free parameter in the model is the frictional time constant. Comparison with observed temperature perturbations over zonal currents in the troposphere shows that the frictional time constant is on the same order as the radiative time constant for all these objects. Vertical motions predicted by the model are extremely weak. They are much smaller than one scale height per orbital period, except in the immediate neighborhood of tropospheric zonal currents.

1. Introduction

The Voyager spacecraft have provided a significant body of information on the meteorology of Jupiter, Saturn, and Uranus. In particular, the infrared spectroscopy experiment has yielded information on atmospheric thermal structure while the imaging experiment has obtained winds by means of cloud top tracking. In the work reported here, a simplified radiative-dynamical model is developed and used as a diagnostic tool to investigate the behavior of the thermal structure in the upper tropospheres and stratospheres of the outer planets and to examine the relationship of that structure to the observed wind fields.

A number of models of the radiative equilibrium temperature structure for the outer planets have been developed. Much of the earlier work consisted of calculations of radiative-convective equilibrium temperature profiles for spatially and annually averaged conditions (Wallace *et al.*, 1974; Wallace, 1980; Appleby and Hogan, 1984). More recently, radiative-convective temperature structure has been obtained as a function of season and latitude for Saturn, Uranus, and Neptune (Wallace, 1983; Wallace, 1984, Bézard *et al.*, 1984; Bézard and Gautier, 1985 and 1989). Friedson and Ingersoll (1987) have applied a radiative-

convective- dynamical model to Uranus in which meridional redistribution of heat was introduced with a parameterized baroclinic wave formulation, while certain aspects of the zonally symmetric circulation of Uranus have been modeled by Friedson (1987) and by Hou and Goody (1988).

Gierasch *et al.* (1986) employed a set of linearized balance equations to investigate certain aspects of the relationship between the observed temperature and wind fields on Jupiter. A similar model was used by Flasar *et al.* (1987) in an application to Uranus. In the latter study, the observed temperature as a function of latitude was imposed at the lower boundary, and the calculated zonal wind field was compared with the observed zonal winds. Radiative forcing was not included in the model. In the present work we have extended the model to include realistic radiative forcing and have applied it to the atmospheres of Jupiter, Saturn, and Uranus. We have addressed two aspects of the temperature fields and circulation. The first is the remarkably small pole-to-equator temperature gradients found in the upper tropospheres and lower stratospheres of all three planets despite the strong latitude dependence of the insolation at any given time. The second concerns the relationship between the observed temperatures and winds; the two sets of observations are used to infer information on frictional damping times.

In the following section, the dynamical model is presented, and the methods used to calculate the radiative forcing are discussed. In Section 3 we consider circulations with radiative forcing only, and examine the cases when the radiative time constant is both comparable to and significantly longer than the orbital period of the planet. In Section 4 we simulate mechanical forcing from deeper layers by imposing the observed wind as a function of latitude as a lower boundary condition. Finally in Section 5 we summarize our results and conclusions.

2. Formulation.

A. Notation and coordinates.

Since the linear model we employ is well known (Leovy, 1964; Holton, 1975) we shall be very brief. The notation will be standard. Temperature will be written $T(\theta, p, t)$, where

θ, p and t are latitude, pressure and time. A reference temperature profile $T_0(p)$, to be defined in Section D below, will be based on horizontally averaged heating. We shall refer to a scale height based on T_0,

$$H = \frac{RT_0}{g}, \tag{1}$$

where R is the gas constant and g is the acceleration of gravity. We assume the ideal gas equation, so that $p = \rho RT$. For vertical coordinates we shall employ p and also, where convenient, z, where

$$dz = -\frac{dp}{p}. \tag{2}$$

Thus z is a "Log p" coordinate. Where convenient we shall employ, in addition to the latitude θ, the meridional coordinate

$$y = \sin\theta. \tag{3}$$

The mean planetary radius will be denoted by a. The Coriolis parameter will be denoted by $f = 2\Omega \sin\theta$, where Ω is the planetary rotation rate. Flow velocities in the eastward, northward and upward directions will be denoted by u, v, and $w = H\ Dz/Dt$.

B. Equations of motion.

The linearized equations of motion are

$$\frac{\partial u}{\partial t} - fv = \frac{u_E - u}{t_F}, \tag{4}$$

$$fu + \frac{1}{a}\frac{\partial \Phi}{\partial \theta} = 0, \tag{5}$$

$$\frac{\partial \Phi}{\partial z} = RT, \tag{6}$$

$$\frac{1}{a\cos\theta}\frac{\partial}{\partial \theta}(\rho_0 v \cos\theta) + \frac{1}{H}\frac{\partial}{\partial z}(\rho_0 w) = 0, \tag{7}$$

$$\frac{\partial T}{\partial t} + \frac{N^2 H}{R} w = \frac{T_E - T}{t_R}. \tag{8}$$

The coefficients in these equations are evaluated from the mean thermal structure. For example, $\rho_0 = p/RT_0(p)$, and the Brunt frequency is given by

$$N^2 = \frac{g}{H}\left(\frac{1}{T_0}\frac{\partial T_0}{\partial z} + \frac{R}{c_p}\right). \tag{9}$$

Forcing and dissipation are formulated in terms of equilibrium values and damping time constants in both the zonal momentum equation and the heat equation. $T_E(\theta, p, t)$ is analogous to the seasonally varying (but diurnally averaged) instantaneous radiative equilibrium temperature. It will be precisely defined in Section D. The momentum forcing term u_E will not be used in our experiments, but is displayed for symmetry. The time constants t_E and t_F can be functions of height.

Equation (7) permits a streamfunction to be defined. Let

$$\rho_0 v \cos\theta = \frac{1}{H}\frac{\partial \psi}{\partial z}, \tag{10}$$

$$\rho_0 w \cos\theta = -\frac{1}{a}\frac{\partial \psi}{\partial \theta}, \tag{11}$$

We shall express solutions as Fourier series in time; for example,

$$\psi = \Re\Big\{\sum_{n=0}^{N} \psi^{(n)} \exp(2\pi i n t/P)\Big\}, \tag{12}$$

where P is the orbital period. Time differentiation combined with damping leads to the following factors in equations (4) and (8):

$$\begin{aligned} D_R^{(n)} &= \frac{1}{t_R} + \frac{2\pi i n}{P}, \\ D_F^{(n)} &= \frac{1}{t_F} + \frac{2\pi i n}{P}. \end{aligned} \tag{13}$$

Combining equations (4) - (8) yields an equation for each Fourier component of ψ:

$$\begin{aligned} &\frac{N^2 H^2}{4\Omega^2 a^2}\frac{\partial^2 \psi^{(n)}}{\partial y^2} + \frac{y^2}{1-y^2} D_R^{(n)} p^2 \frac{\partial}{\partial p}\left(\frac{1}{D_F^{(n)}}\frac{\partial \psi^{(n)}}{\partial p}\right) \\ &\qquad = \frac{y}{\sqrt{1-y^2}}\frac{\rho_0 H}{2\Omega t_R} p\left[\frac{\partial u_{ET}^{(n)}}{\partial p} - t_R D_R^{(n)}\frac{\partial}{\partial p}\left(\frac{u_E^{(n)}}{t_F D_F^{(n)}}\right)\right]. \end{aligned} \tag{14}$$

The thermal forcing is expressed in terms of a thermal wind shear based on the instantaneous radiative equilibrium temperature:

$$f p \frac{\partial u_{ET}}{\partial p} = \frac{R}{a}\frac{\partial T_E}{\partial \theta}. \tag{15}$$

The left side of (14) involves an elliptic operator written with dimensionless coefficients. The coefficient of the first term is the square of the ratio of a deformation radius, $NH/2\Omega$, to the planetary radius. For the cases of interest this ratio is much less than unity. Equation (10) shows that to order of magnitude $v \approx \psi/\rho_0 H$. Inspection of (14) thus shows that thermal forcing will produce $v \approx u_{ET}/\Omega t_R$ (provided that the ratio of the D's is of order unity). Near the equator, however, $y \longrightarrow 0$, Coriolis forces become weak, and the amplitude of ψ is larger. This is the low latitude Hadley regime, whose dimensions and amplitude have been discussed by, for example, Schneider and Lindzen (1977). Further discussion of the behavior of solutions will be presented in the context of specific cases.

C. Boundary conditions.

At the top of the atmosphere and at the poles there must be no mass flux into the system, and therefore we require

$$\psi(p = 0, y, t) = \psi(p, y = -1, t) = \psi(p, y = 1, t) = 0. \tag{16}$$

The boundary condition at the base of the system involves fundamental questions about the degree to which the middle atmosphere circulation can be uncoupled from that of the lower atmosphere. For the moment, we shall simply specify three possibilities. If, in some manner, the vertical velocity is specified at the base, then (11) gives

$$\frac{\partial \psi(p_{base}, y, t)}{\partial y} = -a\rho_0 w. \tag{17}$$

For example, if $w = 0$ is specified, (16) and (17) lead to $\psi = 0$ at the base.

If data exist determining the latitudinal distribution of temperature at the base, then one would rearrange (8) to give

$$w(p_{base}, y, t) = \frac{R}{N^2 H}\left(-\frac{\partial T}{\partial t} + \frac{T_E - T}{t_R}\right). \tag{18}$$

In this case, when (17) is integrated to give ψ it is possible that a net mass flux through the lower boundary will be discovered. Since the boundary is defined to be at a fixed pressure, the net mass flux would represent an error either in the data or in T_E, and a correction would need to be made.

A final possibility is that either observational data or modelling of the lower atmosphere give the zonal velocity at the boundary. Then (4) and (10) give

$$p\frac{\partial\psi(p_{base},y,t)}{\partial p} = \frac{\rho_0 H\cos\theta}{f}\left(-\frac{\partial u}{\partial t}+\frac{u_E-u}{t_F}\right). \tag{19}$$

In this case the vertical velocity at the base will emerge from the solution.

D. Radiative forcing.

The heat equation (8) with radiation in a general form is

$$\frac{\partial T}{\partial t}+\frac{N^2H}{R}w = \frac{1}{\rho c_p}(Q_{IR}+Q_S), \tag{20}$$

where $Q_{IR}(p,y,t)$ denotes infrared energy deposition per unit volume and time (usually negative, representing cooling) and Q_S denotes solar heating. Let the annual mean be denoted by an overbar, for example, $\overline{Q}_S(p,y)$. Notice that Q_S is at most a very weak function of temperature (through the dependence of absorption coefficients on the temperature) but that Q_T is a strong one, since it is proportional to the Planck function. The annual average radiative equilibrium temperature $\overline{T}_E(p,y)$ is the solution of

$$\overline{Q}_{IR}+\overline{Q}_S = 0. \tag{21}$$

Recall that $T_0(p)$ is the area weighted horizontal average of $\overline{T}_E(y,p)$. Now assume that the infrared term can be expanded in terms of the local temperature, and define the radiative time constant by writing

$$\begin{aligned} Q_{IR} &= \overline{Q}_{IR}+\frac{\partial Q_{IR}}{\partial T}(T-\overline{T}_E) \\ &= \overline{Q}_{IR}-\frac{\rho c_p}{t_E}(T-\overline{T}_E). \end{aligned} \tag{22}$$

This requires the neglect of exchange terms in the formulation of the radiative heating. This type of approximation is discussed by Goody and Yung (1988). Next, we write the time variations of the solar heating in terms of $T_E-\overline{T}_E$, which constitutes the definition of T_E:

$$Q_S = \overline{Q}_S+\frac{\rho c_p}{t_E}(T_E-\overline{T}_E). \tag{23}$$

Thus $\overline{T}_E(y,p)$ is a true radiative equilibrium solution, but $T_E(y,p,t)$ contains a time varying part which is directly proportional to the solar heating perturbations. Note that T_E is not the instantaneous radiative equilibrium temperature. Under this formulation the only linearization is in the infrared terms. As the final step in the formulation of the approximation, the coefficients in the foregoing equations, which are functions of $T_E(p,y)$, are instead evaluated only as functions of $T_0(p)$. Inserting (22) and (23) into (20), using (21), then gives the heat equation (8).

E. Solar heating by gaseous absorption.

We follow the formulation of Bézard *et al.* (1984) for the strong methane bands at 3.3, 2.3 and 1.7 μm. For the weak methane bands at wavelengths less than 1.7 μm we follow Wallace *et al.* (1974). We find

$$Q_S = \rho g \mu_0 \sum_{i=1}^{3} \frac{d\ln(\hat{p}_i N_1)}{dp} F_{\odot i} A_i \left[1 + \left(\frac{A_i d_i \mu_0}{2 S_i \gamma_i \hat{p}_i N_i}\right)^{\frac{1}{2}}\right]^{-1}$$
$$+ \rho g \frac{dN_1}{dp}\left(\overline{F}_{\odot a}\Delta\nu_a C_a e^{-C_a N_1/\mu_0} + \overline{F}_{\odot b}\Delta\nu_b C_b e^{-C_b N_1/\mu_0}\right). \qquad (24)$$

In this expression μ_0 is the cosine if the solar zenith angle, the subscript i labels the particular band, and $F_{\odot i}$ is the specific flux of the sun (per inverse centimeter) at the i^{th} band. N_i is the column abundance of the gas (for $i = 1,\ 2,\ 3$ always methane) down to the level p, expressed in cm-amagats. $\hat{p}_i$ is the Curtis-Godson (abundance weighted) mean pressure along the beam path from space to the level p. Band parameters are given in Table I. The second line of (24) gives the heating due to the weak bands. We averaged the band parameters of Wallace *et al.* (1974) over two spectral intervals, $\Delta\nu_b$ from 13514 cm^{-1} to 9804 cm^{-1} and $\Delta\nu_a$ from 9434 cm^{-1} to 6667 cm^{-1}. The $\overline{F}_{\odot}$'s are the average specific solar fluxes over the intervals. The absorption parameters, averages of those from Wallace *et al.*, are $C_a = 1.36 \times 10^{-4}$ and $C_b = 4.8 \times 10^{-5}$ (cm-amagat)$^{-1}$.

F. Infrared heating.

We evaluate cooling due to emission from the 7.7, 12.2 and 13.7 μm bands of methane, ethane and acetylene, using band parameters from Cess and Chen (1975). Here also we

consider only the radiation path from the level of interest directly to space. In contrast, infrared heating due to hydrogen opacity requires an exchange formulation. We normally used 64 levels between 1 bar and space, assuming that the Planck function at each frequency is piecewise linear. The spectrum between 50 cm^{-1} and 2000 cm^{-1} was evaluated at 20 cm^{-1} resolution. The collision induced absorption coefficients for H_2-H_2 and H_2-He collisions were taken from Bachet *et al.* (1983), Cohen *et al.* (1982) and Dore *et al.* (1983). Our expression for the infrared heating is

$$Q_{IR} = -\rho g \sum_{i=4}^{6} \frac{d\ln(\hat{p}N_i)}{dp} \pi B_i A_i \left[1 + \left(\frac{A_i d_i}{2 S_i \gamma_i \hat{p} N_i} \right)^{\frac{1}{2}} \right]^{-1} + Q_H, \qquad (25)$$

where Q_H is the hydrogen contribution, B_i denotes the Planck function at band i, the band locations and parameters are given in Table 1, and a diffusivity factor of 2/3 has been used to relate the column band transmission to the flux transmissivity (Goody and Yung, 1989).

3. Radiatively Forced Circulation

A. Radiative calculations.

We shall first consider the circulation resulting from radiative forcing only. The lower and upper boundaries of the model are placed at the 1 bar and 10^{-6} bar levels, respectively. The zonal wind u is set equal to zero on the lower boundary while the meridional stream function ψ is constrained to vanish at the upper boundary. The annual means and the first three harmonics are retained in the Fourier series representations of the seasonal variations of the independent variables. A 64 by 64 grid of points, equally spaced in log p and sine latitude, is used to represent the spatial dependences in the meridional plane.

In calculating $T_E(y,p,t)$ and the radiative time constant t_R, we have included only the absorption of solar energy by gaseous methane, while the infrared emission includes contributions from collision- induced hydrogen, methane, ethane, and acetylene opacities. Latitude independent vertical profiles of the hydrocarbons are used. For Jupiter and Saturn, methane mole fractions are essentially constant over the relevant height range with values of 1.4×10^{-3} and 4.0×10^{-3} respectively. For Uranus, the CH_4, C_2H_2, and

C_2H_6 profiles in the stratosphere are taken from a photochemical model (Romani, 1988; Pollack, et al., 1987) with the methane CH_4/H_2 mixing ratio at the tropopause fixed at the saturation value. In the troposphere, the CH_4 is assumed to be saturated at all levels. In the case of Neptune, the stratospheric hydrocarbon proflies are taken from a model of Romani and Atreya (1988) in which the CH_4/H_2 mixing ratio has a value of 0.02 at the 10 mbar level and is determiend by the photochemistry above this level. Below the 10 mbar level, the mixing ratio is maintained at 0.02 until the saturation level is reached, and at deeper levels the saturation curve is followed. To simulate the efficient redistribution of heat at levels deeper than those treated in this model, the annual mean T_E was assumed to be independent of latitude at the lower boundary. To account for the infrared flux from deeper levels, the temperature was extrapolated adiabatically for pressures greater than 1 bar.

The temporally and spatially averaged radiative equilibrium temperature profiles obtained for Jupiter, Saturn, and Uranus are shown in Fig. 1. These profiles were used to approximate the reference profile $T_0(p)$ defined in the previous section. Also shown for comparison are radio occultation ingress profiles from the Voyager 1 encounters with Jupiter (Lindal *et al.*,1981) and Saturn (Lindal *et al.*,1985) and the Voyager 2 encounter with Uranus (Lindal *et al.*,1987). The purpose of the comparisons is to verify that the radiative equilibrium temperatures have the correct gross behavior. For purposes of this study, no attempt has been made to bring the calculations into exact agreement with observations. Our result for Saturn is more nearly in agreement with the occultation profile in the stratosphere than is the case for Jupiter and Uranus, where the calculated profiles are systematically too cold. Similar results have been obtained for Saturn by Bézard and Gautier (1985), and the relatively warm temperatures can be attributed to the large methane mole fraction used (approximately 4 times the equivalent solar value), which is consistent with the value obtained by Courtin *et al.*(1984) from an analysis of Voyager IRIS data. Although we do not include the results of dynamical modelling for Neptune in this paper, the mean radiative equilibrium profile for that planet was calculated and is displayed in Fig. 1. The warm upper stratosphere obtained for Neptune is the result of the relatively large stratospheric methane abundance used. For Jupiter and Saturn

the underestimation of stratospheric temperatures by models that include solar absorption by gaseous methane only has been noted by various authors (Appleby and Hogan, 1984; Bézard and Gautier, 1989). By adding appropriately chosen additional heating, usually attributed to atmospheric aerosols, it is possible to force agreement between the models and the measurements. In the present work, we are interested primarily in latitudinal gradients in T_E and have elected to consider only heating due to gaseous absorption. If there is additional heating that is independent of latitude, there will be little effect on the circulation; however, if an absorbing aerosol exists that varies strongly with latitude, then the flow may be significantly altered. Since the possible latitude dependence of absorbers does not appear to be well constrained at the present time, such effects have not been included here.

The globally and annually averaged radiative time constants used in the model are shown as functions of pressure in Fig. 2. In all cases, the time constants were obtained by perturbing the temperature profile by a fixed amount at all levels and calculating the resultant change in Q_{IR} at each level. When the radiative time constant is smaller than the orbital time, specifically, when the parameter $2\pi t_R/t_{orb}$ is of order unity or smaller, we anticipate a stronger seasonal response than for the case when this parameter is significantly larger than unity. Jupiter and Saturn both fall in the first category while Uranus is an example of the second; both cases will be considered below.

B. Circulation with $t_R > t_{orb}$.

We shall illustrate this case by discussing Uranus. As Fig. 2 shows, $2\pi t_{orb}/t_R$ exceeds 10 through most of the height interval of concern. In Fig. 3a, the meridional cross section of the annual mean radiative equilibrium temperature for Uranus is displayed. The most striking feature of this temperature field is the very weak dependence on latitude at all levels. In the upper troposphere and stratosphere, the polar regions are only slightly warmer than the equator. The behavior results from a combination of two factors characteristic of this model. At the deeper levels, the assumption that the annual mean T_E is constant along the lower boundary forces T_E to be nearly latitude independent at levels immediately above the boundary. In the stratosphere, the weak latitude dependence is a direct

consequence of the fact that most of the solar heating in this region results from absorption in the weak CH_4 bands. Because these bands are essentially optically thin, the heating is nearly independent of the solar zenith angle for pressure levels less than ~100 mbar. Therefore, the annual mean solar heating is dependent on the integrated solar irradiance at the top of the atmosphere and not the locally normal component of the solar flux. It can be shown that the solar irradiance integrated over an orbital period is independent of latitude. This is true even for an elliptical orbit since the Kepler's law requirement that equal areas be swept out in equal times by the radius vector between the sun and planet just compensates for the inverse square dependence of the solar irradiance. This result would also hold if a latitude-independent absorbing aerosol were present, provided it is optically thin.

The meridional cross section of the difference $\delta T = T - T_E$ between the actual atmospheric temperature and the annual mean is shown in Fig. 3b. Although there is a tendency toward cancellation of the equator-to-pole gradients in the annual mean T_E, the differences are very small at all latitudes and pressure levels. The smallness of the T_E gradients, which provide the sole forcing for the circulation in this case, results in a very weak meridional circulation. As a consequence, departures of the temperature field from the annual mean radiative equilibrium values are almost negligible.

The stream function for the annual mean meridional circulation is shown in Fig. 4a and the vertical velocity calculated from the stream function is given in Fig. 4b. Note that the principal circulation is confined to a low-latitude cell with rising motion mainly between 10 and 30 degrees latitude in both hemispheres and with subsidence primarily at the equator. The anticipated scale of the meridional circulation is discussed further below. The accompanying zonal mean winds reach only a few meters per second, much smaller than the maximum wind speeds of ~100 m s^{-1} obtained from cloud tracking in the Voyager images. Clearly, some additional forcing must be present, possibly mechanical forcing from below.

Because of the 94 degree obliquity of Uranus, the seasonally varying component of the radiative forcing is large, as shown in Fig. 5. The meridional cross section for T_E is

displayed for northern hemisphere solstice and equinox in Figs. 5a and 5b respectively. The large hemispheric gradient occurring at solstice is substantially attenuated in this representation because of the truncation of the Fourier series after three harmonics. At equinox, T_E is nearly symmetric about the equator with low latitudes slightly warmer than higher latitudes at all pressure levels.

The meridional circulation for solstice conditions is shown in Fig. 6. A single weak cell is found with rising motion in the summer (northern) hemisphere and subsidence in the winter hemisphere. The most intense part of the circulation is again found equatorward of 30 degrees latitude. Even though the annual amplitude of T_E is large, the response of the atmospheric temperature field is small as a direct consequence of the radiative time constant exceeding the orbital period of the planet. The balance in the thermodynamic energy equation (8) is primarily between the time-derivative of the temperature and the diabatic heating, so the resulting temperature is essentially that which would be obtained from a time-marching radiative equilibrium calculation.

C. Circulation with $t_R \sim t_{orb}$.

The radiative time constants for both Jupiter and Saturn are comparable to their orbital periods as shown in Fig. 2. Because Saturn has an obliquity of $\sim$27 degrees and hence a significant seasonal radiative forcing, we have chosen to consider results for that planet in detail here.

The annual mean radiative equilibrium temperature is shown in Fig. 7. Again we find little horizontal contrast, with the equator slightly warmer than the poles. The resulting annual mean meridional circulation is shown in Figs. 8 a and b in terms of the stream function and the vertical velocity respectively. A double cell configuration is obtained consisting of rising motion at low latitudes with maximum subsidence occuring at quite high latitudes. The departure of the temperature field from radiative equilibrium, as shown in Fig. 8 c, does not exceed approximately 0.1 K.

Results for northern hemisphere solstice are given in Fig. 9. The radiative forcing T_E (Fig. 9 a) shows a strong hemispheric asymmetry with maximum temperatures at the summer pole and minimum values near the winter pole. The temperature response of the

atmosphere (Fig. 9 b) shows a more nearly symmetric behavior with weaker gradients. This is a consequence of the phase lag of nearly one season which occurs even when the radiative time constant is of the same order of magnitude as the orbital period. The meridional motion is displayed in Figs. 9 c and 9 d. A diffuse interhemispheric circulation with rising motion in the summer hemisphere and downward motion in the winter hemisphere is obtained. The accompanying zonal mean wind field is shown in Fig. 9 e. The resulting broad jets have maximum velocities substantially weaker than those observed.

Results obtained for the northern spring equinox are displayed in Fig. 10. The forcing (Fig. 10 a) is essentially symmetric, but the response of the atmospheric temperature field (Fig. 10 b) is highly asymmetric. This is a consequence of the nearly 90 degree phase lag so the response more nearly reflects the forcing near solstice. The meridional flow (Figs. 10 c and 10 d) consists of a two-cell structure with rising motion at low latitudes and downward motion poleward of 30 degrees latitude in each hemisphere. The mean zonal flow, Fig. 10 e, consists of prograde and retrograde jets in the northern and southern hemispheres respectively. In both hemispheres, a local minimum in wind speed occurs at mid latitudes. The high-latitude maxima result from the increase in the latitudinal temperature gradients at high latitudes while those at low latitudes are a consequence of the decrease in the magnitude of the Coriolis parameter with decreasing latitude.

D. Radiatively forced meridional circulation.

Here we shall comment on the geometry and strength of the radiatively forced circulations. Inspection of (14) reveals that the two terms in the elliptic operator on the left hand side are of the same order when

$$y^4 \sim \frac{D_F}{D_R} \frac{N^2 H^2}{4\Omega^2 a^2}, \tag{26}$$

where we have assumed that the vertical scale of the streamfunction ψ is on the order of a scale height. This relation gives the linear Hadley cell width discussed by Schneider and Lindzen (1977), for example. For values of y smaller than these, the first term on the left hand side of (14) dominates, and it is easy to show that the vertical velocity is then given

to order of magnitude by

$$w \sim \frac{H}{t_R} \frac{R\Delta T_E}{N^2 H^2}, \tag{27}$$

which states that adiabatic compression balances radiative heating. In this relation, ΔT_E is the horizontal variation of T_E within the Hadley regime. It is this factor that makes the vertical velocities extremely small. The combination $N^2 H^2/R$ is on the order of T_E (unless the atmosphere is close to adiabatic, which is not the case within the upper tropospheres and stratospheres). Thus if ΔT_E were on the order of the full temperature, the vertical velocity would be about one scale height per radiative relaxation time. But in fact ΔT_E is an extremely small fraction of T_E itself, and therefore even within the low latitude Hadley cell, w is much smaller than H/t_R.

The Hadley cells are apparent in the foregoing Figures. Their precise dimensions of course depend on the detailed shape of the forcing functions. Poleward of the Hadley cells, the meridional circulation is weaker still. The second term on the left hand side of (14) dominates over the first, and in this case it can be shown that

$$w \sim \frac{H}{t_R} \frac{D_F}{D_R} \frac{R\Delta T_E}{4\Omega^2 a^2}. \tag{28}$$

Assuming that D_F/D_R is not far from unity, this estimate of w is smaller than that within the Hadley cell by

$$\frac{N^2 H^2}{4\Omega^2 a^2},$$

the same small factor which makes the Hadley cells narrow.

4. Mechanically Forced Circulation.

Up to this point we have taken $u = 0$ as a lower boundary condition. We shall now consider numerical experiments in which mechanical forcing at deeper levels is simulated by imposing a non-vanishing $u(\theta)$ at the lower boundary based on values inferred from Voyager images. The object here is to investigate the decay of the jets with height, the behavior of the temperature field, and the meridional circulation in the presence of such forcing. Since the jet structure is observationally defined in greatest detail for Jupiter, we shall use that planet as an example here. The radiative forcing is included in the same manner as in the previous cases considered.

As a basis for comparison, the annual mean meridional circulation for Jupiter, obtained with radiative forcing only, is shown in Fig. 11. The structure consists of two principal cells, one in each hemisphere, with rising motion near the equator and subsidence at higher latitudes.

The mean zonal wind as a function of latitude obtained by Limaye (1986) was imposed at the 1-bar lower boundary with the results shown in Fig. 12. Strictly speaking, the observed wind field pertains to the cloud tops which are believed to lie in the 0.5 to 0.7 bar range. The meridional stream function, displayed in Fig. 12 a, clearly shows the jet-scale circulation cells induced by the mechanical forcing. Rising motion occurs on the equatorward edge of prograde jets. The decay of the zonal winds with height is shown in Fig. 12 b where it can be seen that all but the strongest jets have damped out by the time the 0.005 bar level is reached. Above this level the multi-cell meridional circulation gives way to essentially the two-cell structure associated with the pure radiative forcing (compare with Fig. 11a). The critical levels (where $u = 0$) occur because the solution is a linear superposition of the mechanically forced and radiatively forced circulations.

The effect of the mechanically forced circulation on the atmospheric temperature structure can be seen in Fig. 12 c. The latitudinal gradients reach their maximum values in the upper troposphere and lower stratosphere where rapid decay of the jets occurs. In Fig. 13 we compare the model temperature as a function of latitude at the 0.15 bar level with temperatures for that level retrieved from measurements made with the IRIS instrument on Voyager 2 (Hanel *et al.*, 1979). The temperatures are taken from Gierasch *et al.* (1986). The major features of the measured temperatures are reproduced by the model.

An estimate of the meridional circulation strength in the case when zonal velocities are imposed at the lower boundary can be made from the fundamental equations (4), (10) and (11). For the vertical velocity, we obtain

$$w \sim \frac{H}{t_F} \frac{u}{2\Omega L \sin\theta}, \tag{29}$$

where L is the horizontal scale of the imposed jets. Since t_F is on the same order as t_R (see below) and the Rossby number is not extremely small, it is clear that this circulation

will be larger than (28).

In the model calculation considered here, as in those of the previous section, we assumed that the unknown frictional damping t_F is equal to the radiative time constant t_R at all atmospheric levels. In the present case where $u(\theta)$ is imposed at the lower boundary, it can easily be shown that the amplitude of the resulting latitudinal temperature structure is directly proportional to the ratio t_R/t_F in a first approximation. Therefore, by requiring that the observed wind and temperature fields be consistent with one another, it is possible to estimate the magnitude of t_F. For Jupiter, the temperatures displayed in Fig. 13 demonstrate that the ratio must be about unity for agreement of the model with observation. Notice that there is disagreement near the equator; this is because the model breaks down where Coriolis forces vanish. In fact, this particular model always predicts $u = 0$ exactly on the equator, and if given a boundary condition that is inconsistent, it produces an artificially large meridional streamfunction. In the case of Uranus, the analysis of IRIS data by Flasar *et al.* (1987), using the same model as the present paper but without solar heating, also gave the result $t_F/t_R \sim 1$. For Saturn the situation is complicated by the extremely strong equatorial jet. The zonal wind profile was obtained from Voyager images by Ingersoll *et al.* (1984), and the temperatures retrieved from IRIS data by Conrath and Pirraglia (1983). The results of a numerical experiment with u imposed at the base are displayed in Fig. 13, for the seasonal time of the Voyager flyby . The large value of u at the equator produces a large spurious meridional circulation which contaminates low- and mid-latitudes. However, from the behavior over the jets near 50° N we conclude that a ratio of about unity is also correct in this case. Note that the seasonal temperature asymmetry is reproduced correctly by the model.

For all three planets, the ratio t_R/t_F giving the best fit is found to be of order unity even though t_R varies by almost two orders of magnitude from Jupiter and Saturn to Uranus. This can be regarded as a strong conclusion since the amplitude of the latitudinal temperature structure is essentially proportional to t_R/t_F.

5. Summary and Conclusions.

A simple, linearized radiative-dynamical model with Rayleigh friction and Newtonian

cooling has been applied to the atmospheres of Jupiter, Saturn, and Uranus. While no attempt has been made to simulate detailed dynamical processes on the outer planets, the model has been used as a diagnostic tool to investigate certain aspects of atmospheric thermal structure and circulation. Our principal results are as follows.

The annual mean radiative equilibrium temperatures for each planet are found to be only weakly dependent on latitude at all pressure levels. This occurs at the deeper levels because the annual mean radiative equilibrium temperature T_E has been constrained to be constant on the lower boundary. In the upper troposphere and stratosphere the small latitudinal gradients in T_E are a direct consequence of the dominance of solar heating in the model by the weak bands of CH_4 which are optically thin over most of the upper atmosphere. To a first approximation, this results in an instantaneous heating which is independent of solar zenith angle and an annual mean solar heating independent of latitude.

When the radiative time constant is long relative to the orbital period, as is the case for Uranus, the atmospheric temperatures remain close to the annual mean radiative equilibrium values even though the seasonal amplitude of the radiative forcing is large. The resulting residual circulation is weak and does not contribute significantly to the meridional heat transport. In the case of Saturn where the radiative time constant is comparable to the orbital period and there is a significant seasonal radiative forcing, some seasonal response in the temperature field occurs. However, the resulting circulation is also weak. We conclude that the atmospheric temperatures in both cases lie close to the time-marching radiative equilibrium values, and the relatively weak pole-to-equator gradients are a consequence of the small latitudinal gradients in the annual mean radiative equilibrium temperature field.

By imposing the observed zonal wind field as the lower boundary condition in the model and requiring the latitudinal gradients in the resulting temperature field to agree approximately with those inferred from Voyager IRIS measurements, we are able to estimate the magnitude of the frictional damping time in the model. For all three planets the best fit is found when the frictional damping time is comparable to the radiative time constant even though the latter varies by almost two orders of magnitude from Jupiter

and Saturn to Uranus. Since the mechanism for the frictional damping is not understood, the reason for the approximate equality of the two time scales is unclear. Following the Voyager encounter of Neptune, it will be possible to infer the frictional damping time in a similar way for that planet also. This will be of interest, since the radiative time constants of Uranus and Neptune are comparable, but Neptune has a significantly larger internal heat flux.

Acknowledgments. This work was supported in part by the NASA Planetary Atmospheres Program and by the NASA Voyager Project. We are grateful to Dr. Paul Romani for providing calulations of hydrocarbon profiles in advance of publication.

References

Appleby, J. F. and J. S. Hogan, 1984. Radiative-convective equilibrium models of Jupiter and Saturn. *Icarus,* **59,** 336–366.

Bachet, G., E. R. Cohen, P. Dore and G. Birnbaum, 1983. The translational-rotational absorption spectrum of hydrogen. *Canadian J. Physics,* **61,** 591–603.

Bézard, B. and D. Gautier, 1985. A seasonal climate model of the atmospheres of the giant planets at the Voyager encounter time. I. Saturn's stratosphere. *Icarus,* **61,** 296–310.

Bézard, B. and D. Gautier, 1988. A seasonal climate model of the atmospheres of the giant planets at the Voyager encounter time. II. The Uranus atmosphere. *Icarus,* in press.

Bézard, B., D. Gautier and B. J. Conrath, 1984. A seasonal model of the Saturnian upper troposphere: Comparison with Voyager infrared measurements. *Icarus,* **60,** 274 - 278.

Cess, R. D. and S. C. Chen, 1975. The influence of ethane and acetylene upon the thermal structure of the Jovian atmosphere. *Icarus,* **26,** 444 - 450.

Cohen, E. R., L. Frommhold and G. Birnbaum, 1982. Analysis of the far infrared H_2-He spectrum. *Canadian J. Physics,* **77,** 4933–4941.

Conrath, B. J. and J. A. Pirraglia, 1983. Thermal structure of Saturn from Voyager infrared measurements: Implications for atmospheric dynamics. *Icarus,* **53,** 286–291.

Courtin, R., D. Gautier, A. Marten, B. Bezard, and R. Hanel, 1984. The composition of

Saturn's atmosphere at northern temperate latitudes from Voyager IRIS spectra: NH_3, PH_3, C_2H_2, C_2H_6, CH_3D, CH_4 and the Saturnian D/H isotopic ratio. *Astrophys. J.*, **287**, 899-916.

Dore, P., L. Nencini and G. Birnbaum, 1983. Far infrared absorption in normal H_2 from 77 K to 298 K. *J. Quant. Spect. Rad. Transfer*, **30**, 245–253.

Flasar, F. M., B. J. Conrath, P. J. Gierasch, and J. A. Pirraglia, 1987. Voyager infrared observations of Uranus' atmosphere: thermal structure and dynamics. *J. Geophys. Res.*, **92**, 15,011–15,018.

Friedson, J., 1987. Seasonal zonal mean circulation and thermal structure of Uranus' atmosphere. *Bull. Am. Astron. Soc.*, **19**, 852.

Friedson, J., and A. P. Ingersoll, 1987. Seasonal meridional energy balance and thermal structure of the atmosphere of Uranus: A radiative-convective-dynamical model. *Icarus*, **67**, 456-483.

Goody, R. M. and Y. Yung, 1989. **Atmospheric Radiation.** New edition, in press.

Hanel, R., B. Conrath, M. Flasar, L. Herath, V. Kunde, P. Lowman, W. Maguire J. Pearl, J. Pirraglia, R. Samuelson, D. Gautier, P. Gierasch, L. Horn, S. Kumar, and C. Ponnamperuma, 1979. Infrared observations of the Jovian system from Voyager 2. *Science*, **206**, 952–956.

Hanel, R., B. Conrath, F. M. Flasar, V. Kunde, W. Maguire, J. Pearl, J. Pirraglia, R. Samuelson, D. Cruikshank, D. Gautier, P. Gierasch, L. Horn and C. Ponnamperuma, 1982. Infrared observations of the Saturnian system from Voyager 2. *Science*, **215**, 544–548.

Holton, J. R., 1975. **The Dynamic Meteorology of the Stratosphere and Mesosphere. Met. Monographs, 15,** No. 37, 218 pp.

Hou, A. Y., and R. M. Goody, 1988. The seasonal response of Hadley circulations on Uranus. Paper presented at Uranus Conference, June 28–July 1, Pasadena, CA.

Ingersoll, A. P., R. F. Beebe, B. J. Conrath and G. E. Hunt, 1984. Structure and dynamics of Saturn's atmosphere. In **Saturn,** T. Gehrels and M. S. Matthews, Eds., U. Arizona

Press, pp. 195–238.

Leovy, C. B., 1964. Simple models of thermally driven mesosphere circulation. *J. Atmos. Sci.*, **21**, 327 - 341.

Limaye, S. S., 1986. Jupiter: New estimates of the mean zonal flow at the cloud level. *Icarus*, **65**, 335–352.

Lindal, G. F., G. E. Wood, G. S. Levy, J. D. Anderson, D. N. Sweetnam, H. B. Hotz, B. J. Buckles, D. P. Holmes, P. E. Doms, V. R. Eshleman, G. L. Tyler and T. A. Croft, 1981. The atmosphere of Jupiter: An analysis of the Voyager radio occultation measurements. *J. Geophys. Res.*, **86**, 8721–8728.

Lindal, G. F., D. N. Sweetnam and V. R. Eshleman, 1985. The atmosphere of Saturn: An analysis of the Voyager radio occultation measurements. *Astronomical J.*, **90**, 1136–1146.

Lindal, G. F., J. R. Lyons, D. N. Sweetnam, V. R. Eshleman, D. P. Hinson and G. L. Tyler, 1987. The atmosphere of Uranus: Results of radio occultation measurements with Voyager 2. *J. Geophys. Res.*, **92**, 14,987–15,001.

Pollack, J.B., K. Rages, S. K. Pope, M. G. Tomasko, P. N. Romani, and S. K. Atreya, 1987. Nature of the stratospheric haze on Uranus: Evidence for condensed hydrocarbons. *J. Geophys. Res.*, **92**, 15,037–15,065.

Romani, P. N., 1988. Private communication.

Romani, P. N., and S. K. Atreya, 1988. Methane photochemistry and haze production on Neptune. *Icarus*, **74**, 424-445.

Schneider, E. K. and R. S. Lindzen, 1977. Axially symmetric steady state models of the basic state for instability and climate studies. Part I. Linearized calculations. *J. Atmos. Sci.*, **34**, 263 - 279.

Wallace, L., 1980. The structure of the Uranus atmosphere. *Icarus*, **43**, 243–259.

Wallace, L., 1983. The seasonal variation of the thermal structure of the atmosphere of Uranus. *Icarus*, **54**, 110–132.

Wallace, L., 1984. The seasonal variation of the thermal structure of the atmosphere of

Neptune. *Icarus*, **59**, 357–375.

Wallace, L., M. Prather and M. J. S. Belton, 1974. The thermal structure of the atmosphere of Jupiter. *Ap. J.*, **193**, 481 - 493.

Figure captions.

Figure 1. Temperature profiles based on area-weighted global average heating. Methane, ethane and acetylene concentration profiles are from a global mean model by Romani (1988, personal communication). Aerosols are not included.

Figure 2. Radiative time constant profiles based on the temperature profiles of Figure 1, and on thermal disturbances uniform in height. Within the troposphere, taken constant where T_0 exceeds the effective temperature.

Figure 3. (a) Annual average radiative equilibrium temperature for Uranus. Notice the extremely small latitudinal gradients, in spite of the fact that the net insolation is about 30% greater at the poles than at the equator. (b) The difference $\delta T = T - T_E$, showing the degree of deviation from radiative equilibrium on an annual average.

Figure 4. (a) Uranus annual average stream function ψ. Units gm cm^{-1} s^{-1}. There is rising motion near the poles and sinking near the equator. Note that the mass flow is strongly confined to the Hadley regine at latitudes equatorward of ± 20 degrees. (b) Uranus annual average vertical velocity. Units cm s^{-1}.

Figure 5. (a) Uranus radiative equilibrium temperature T_E at north spring equinox. Units degrees Kelvin. Note the small horizontal gradients. (b) At north summer solstice.

Figure 6. Uranus streamfunction ψ at north summer solstice. Units gm cm^{-1} s^{-1}. This is about 10 times stronger than the annual average circulation.

Figure 7. Annual mean radiative equilibrium temperature T_E for Saturn. Units degrees Kelvin. Again note the small horizontal gradients.

Figure 8. (a) Saturn annual average streamfunction ψ. Units gm cm^{-1} s^{-1}. (b) Annual average vertical velocities. Units cm s^{-1}.

Figure 9. (a) Saturn radiative equilibrium temperature T_E at north summer solstice. (b) Temperature T at north summer solstice. (c) Streamfunction ψ at north summer solstice. Units gm cm^{-1} s^{-1}. (d) Vertical velocity w at north summer solstice. Units cm s^{-1}. (e) Zonal velocity u at north summer solstice. Units m s^{-1}.

Figure 10. (a) Saturn radiative equilibrium temperature T_E at north spring equinox. The

slight asymmetry is due to the elliptical orbit and the resulting small discrepancy between $t = 0$ and orbital longitude = 0. (b) Temperature at north spring equinox. This was approximately the time of the Voyager flybys (see Fig. 13). (c) Streamfunction ψ at the same time. Units gm cm^{-1} s^{-1}. (d) Vertical velocity w, units cm s^{-1}. (e) Zonal wind, units m s^{-1}.

Figure 11. Jupiter annual average streamfunction ψ, with radiative forcing alone. Units gm cm^{-1} s^{-1}.

Figure 12. (a) Jupiter annual average streamfunction ψ, with the observed zonal flow imposed as a lower boundary condition. Units gm cm^{-1} s^{-1}. Notice that this circulation is about two orders of maginitude stronger than the radiatively forced one, within the bottom two or three scale heights. (b) Zonal winds, units m s^{-1}. (c) Temperatures.

Figure 13. IRIS data compared with model predictions for Jupiter and Saturn. These are temperatures at the 150 mb levels. Note the good agreement of the Saturn seasonal effect and the Jupiter zonal jets effects. Poor agreement near the equator, particularly for Saturn, is due to failure of the linear model (see text).

Table 1. Band parameters. From Cess and Chen (1975). Units of temperature are Kelvin.

i	Gas	Band (μm)	$\bar{\nu}$ (cm^{-1})	S $(cm\text{-}amagat)^{-1}$	$A\sqrt{300/T}$ (cm^{-1})	$\gamma\sqrt{T/300}$ $(cm\text{-}atm)^{-1}$	d (cm^{-1})
1	CH_4	1.7	5861	3.0	124	0.075	10.5
2	CH_4	2.3	4220	20	124	0.075	10.5
3	CH_4	3.3	3020	320	124	0.075	10.5
4	CH_4	7.7	1306	185	52	0.075	5.3
5	C_2H_6	12.2	821	34	37	0.102	2.6
6	C_2H_2	13.7	729	800	31	0.090	2.4

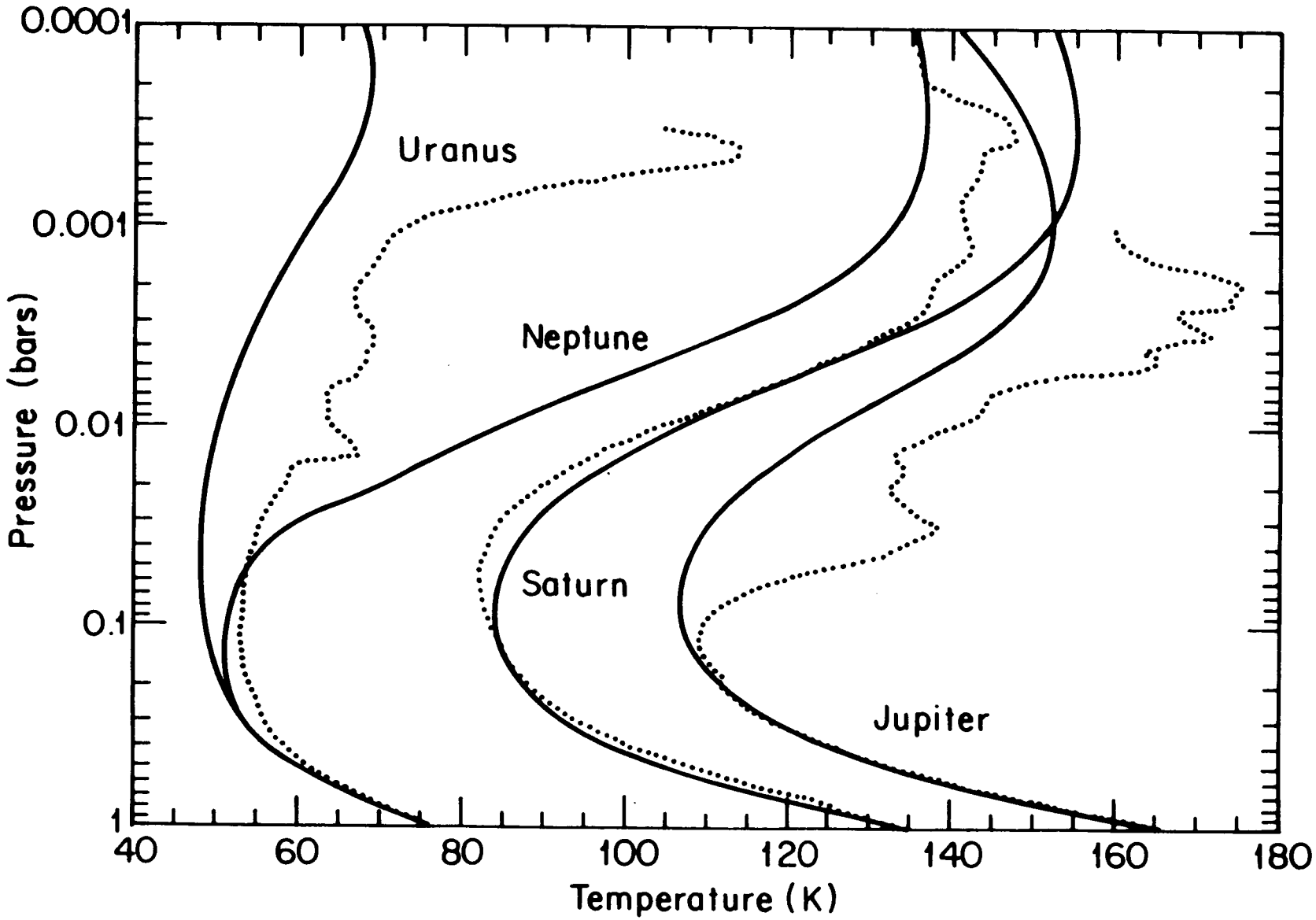
0.0001
0.001
0.01
0.1
1
Pressure (bars)
Uranus
Neptune
Saturn
Jupiter
40
60
80
100
120
140
160
180
Temperature (K)

FIGURE 1

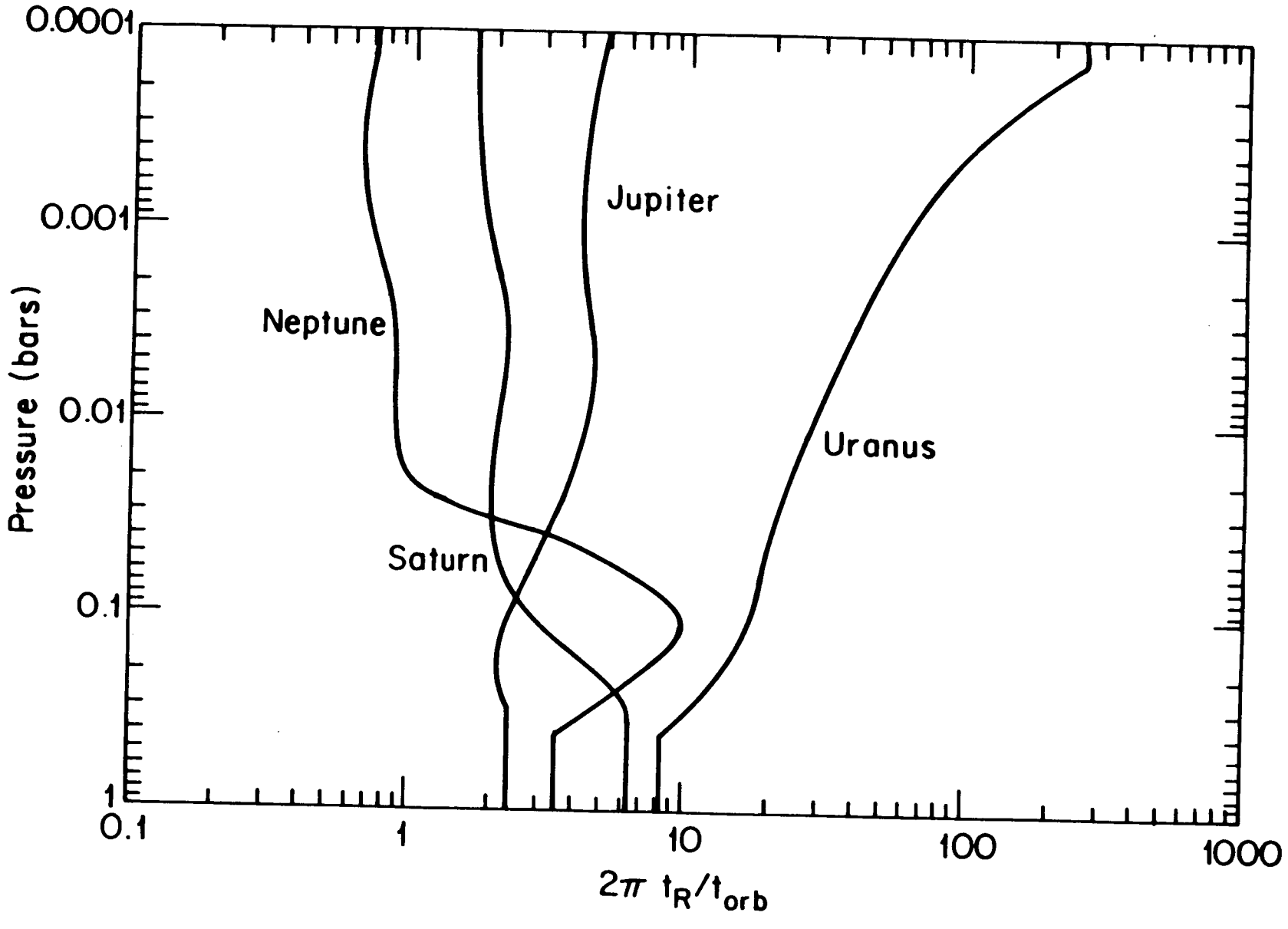
0.0001
0.001
0.01
0.1
1
Pressure (bars)
Neptune
Jupiter
Saturn
Uranus
0.1
1
10
100
1000
2π t_R/t_orb

FIGURE 2

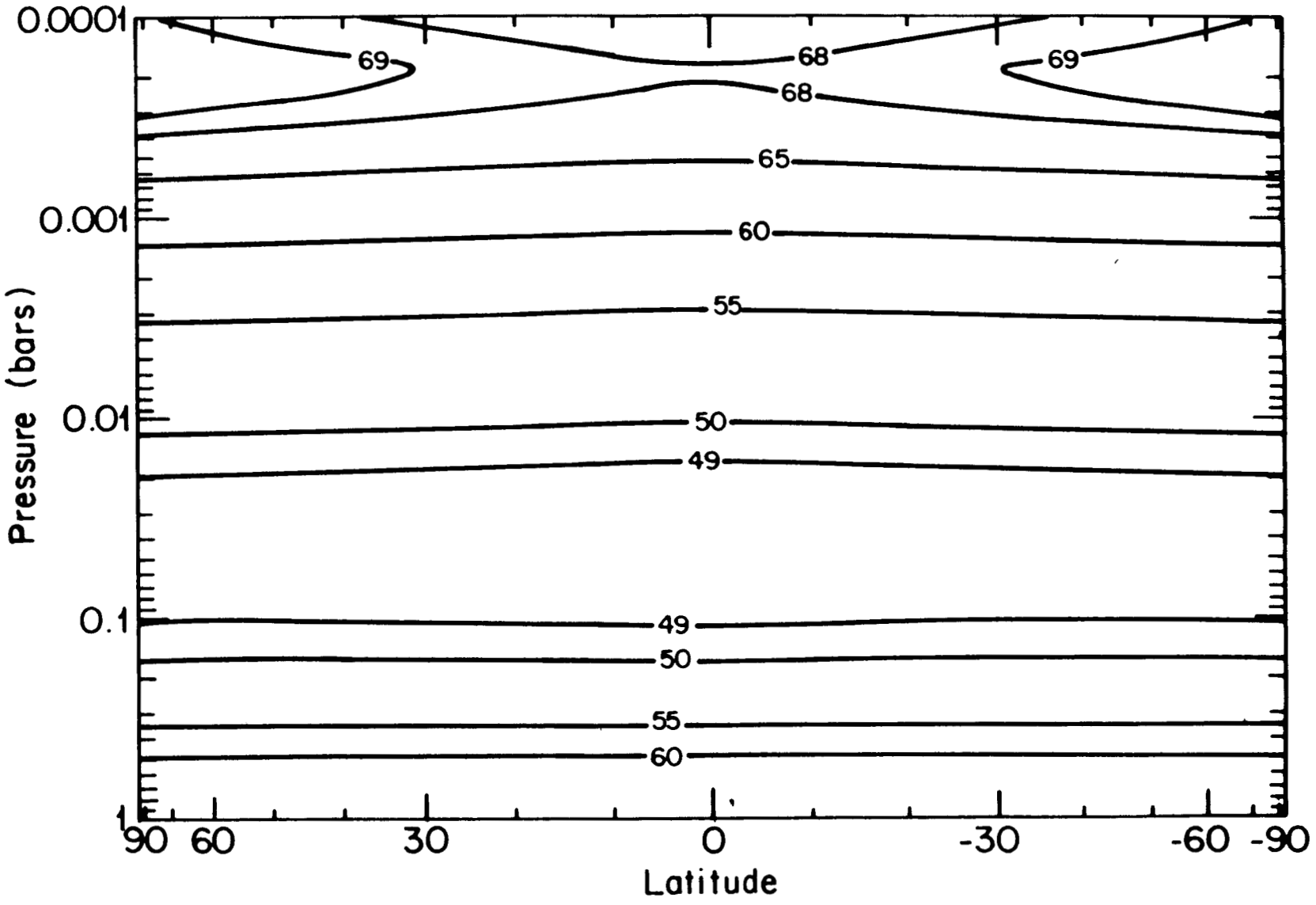
0.0001
0.001
0.01
0.1
1
Pressure (bars)
69
68
68
69
65
60
55
50
49
49
50
55
60
90
60
30
0
-30
-60
-90
Latitude

FIGURE 3a

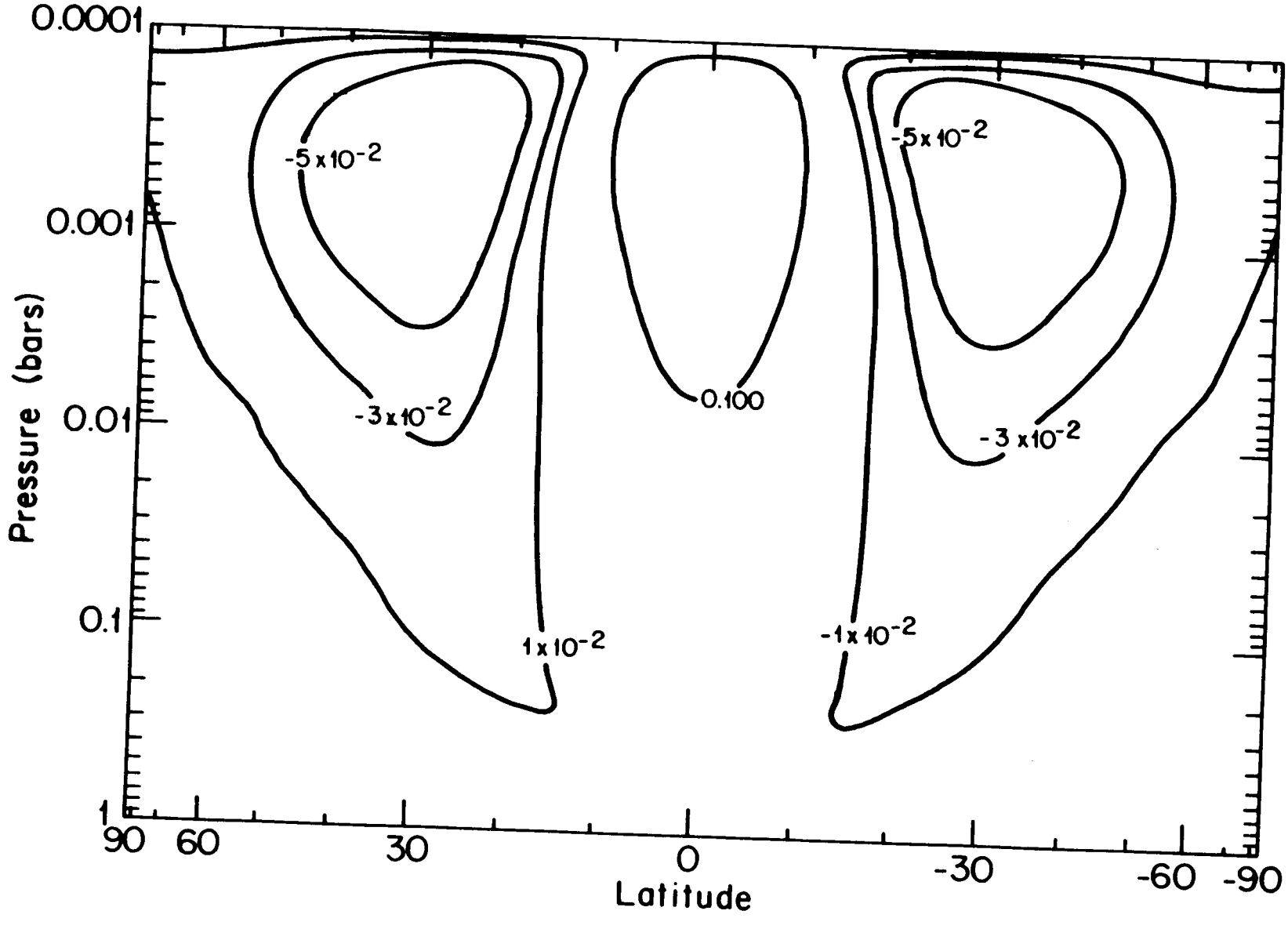
0.0001
0.001
0.01
0.1
1
Pressure (bars)
-5 x 10-2
-3 x 10-2
0.100
1 x 10-2
-1 x 10-2
-5 x 10-2
-3 x 10-2
90
60
30
0
-30
-60
-90
Latitude

FIGURE 3b

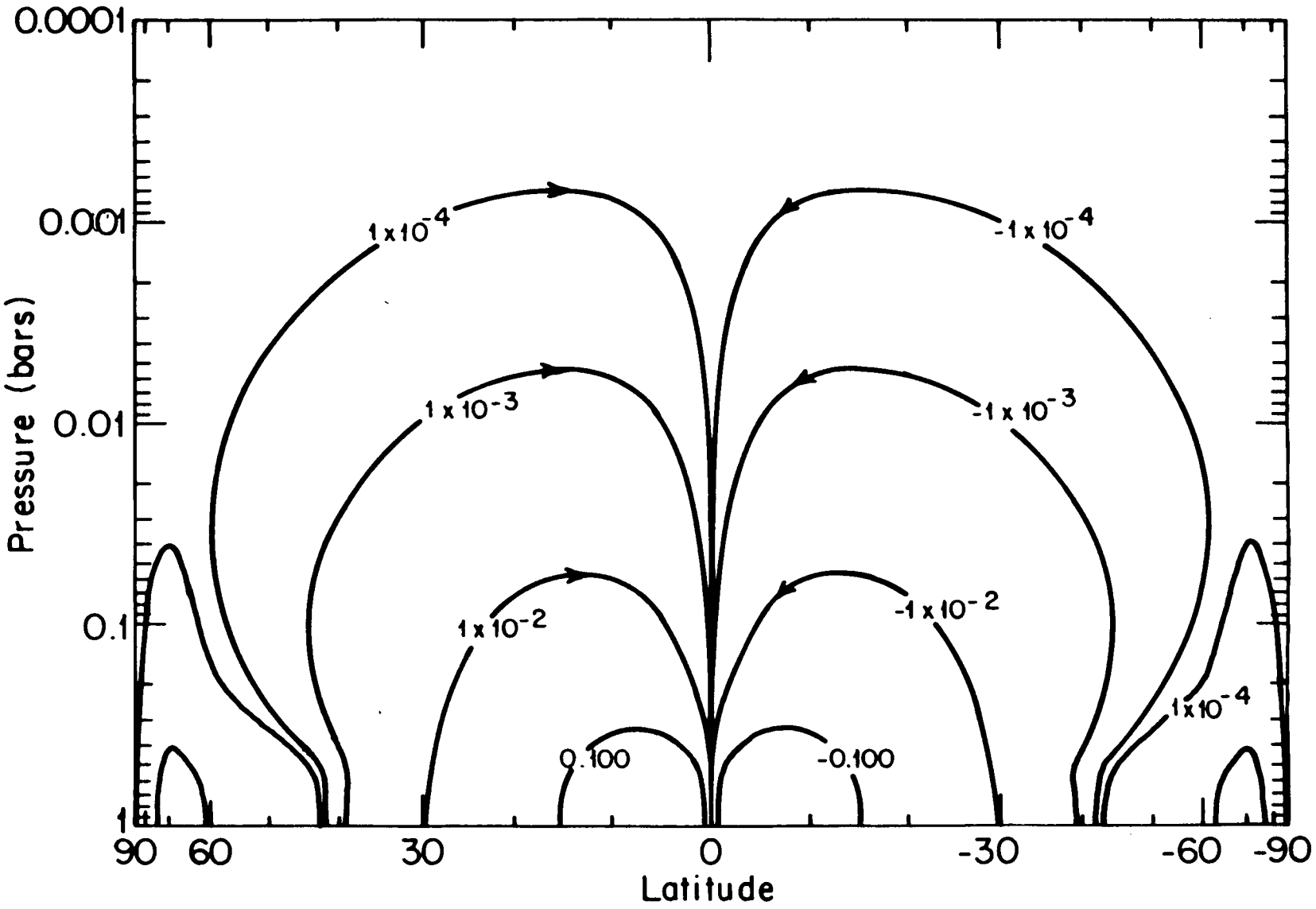
0.0001
0.001
0.01
0.1
1
Pressure (bars)
90
60
30
0
-30
-60
-90
Latitude
1x10-4
-1x10-4
1x10-3
-1x10-3
1x10-2
-1x10-2
0.100
-0.100
1x10-4

FIGURE 4a

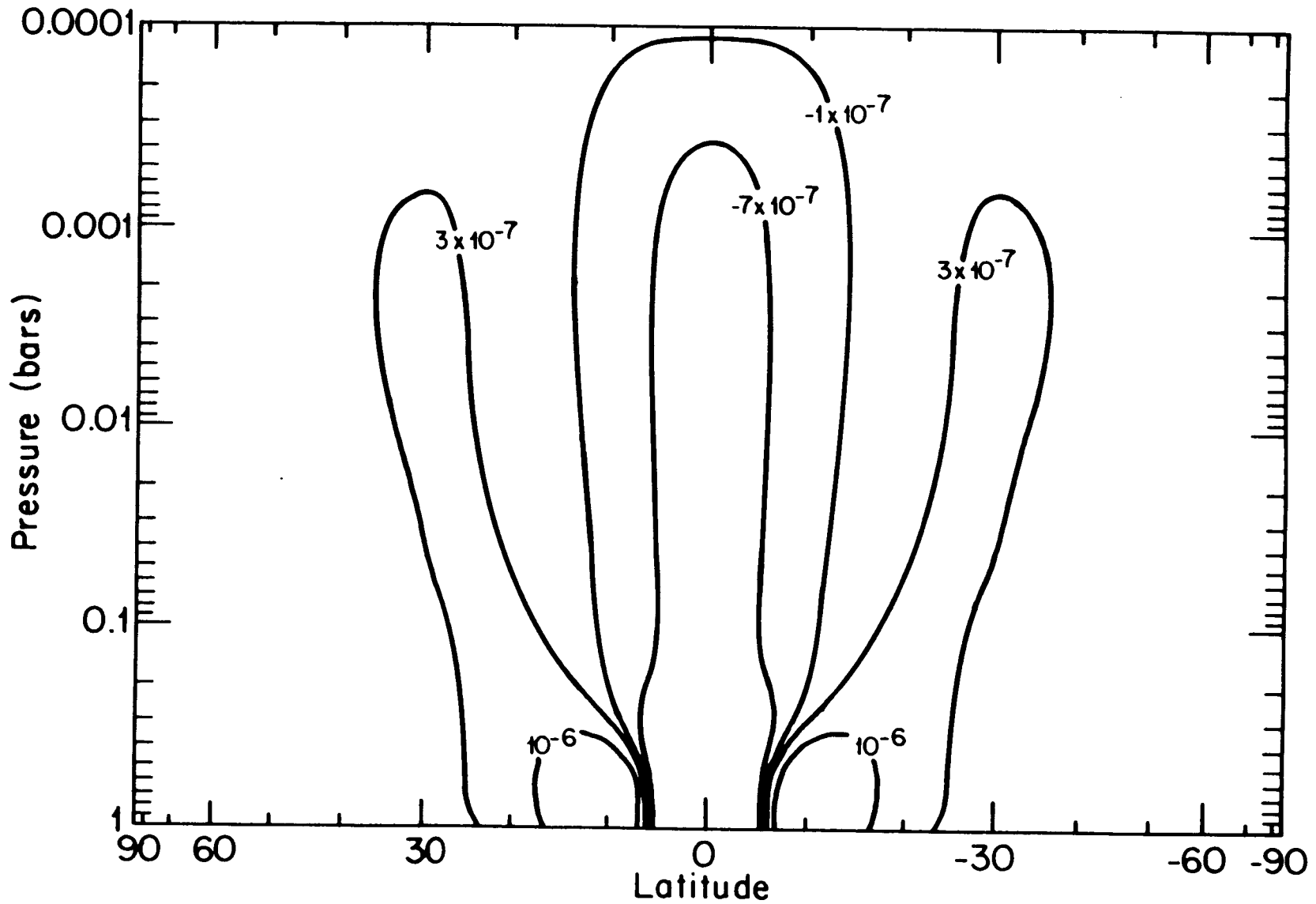
0.0001
0.001
0.01
0.1
1
Pressure (bars)
90
60
30
0
-30
-60
-90
Latitude
-1x10-7
-7x10-7
3x10-7
3x10-7
10-6
10-6

FIGURE 4b

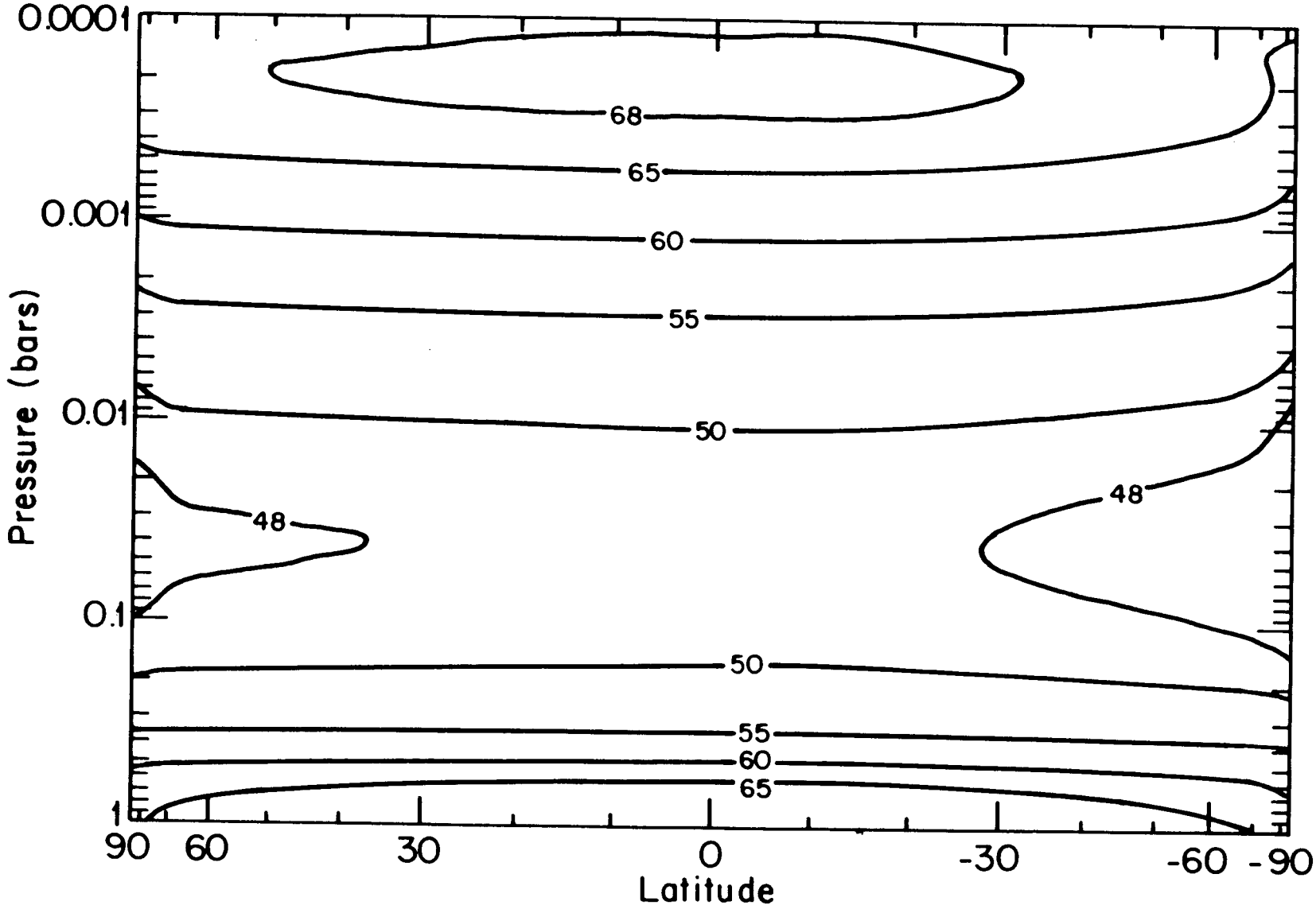
0.0001
0.001
0.01
0.1
1
Pressure (bars)
68
65
60
55
50
48
48
50
55
60
65
90
60
30
0
-30
-60
-90
Latitude

FIGURE 5a

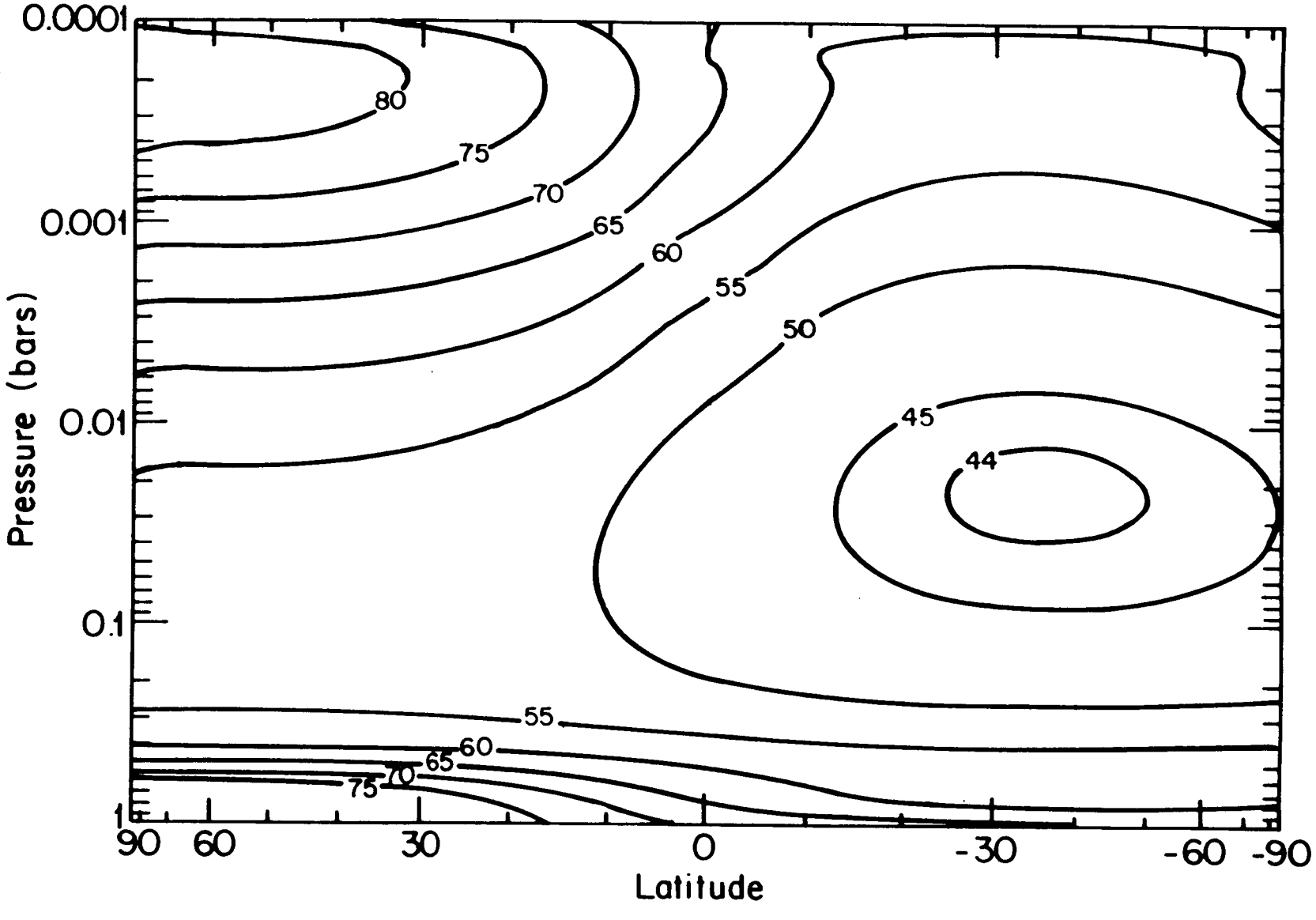
0.0001
0.001
0.01
0.1
1
Pressure (bars)
80
75
70
65
60
55
50
45
44
55
60
65
70
75
90
60
30
0
-30
-60
-90
Latitude

FIGURE 5b

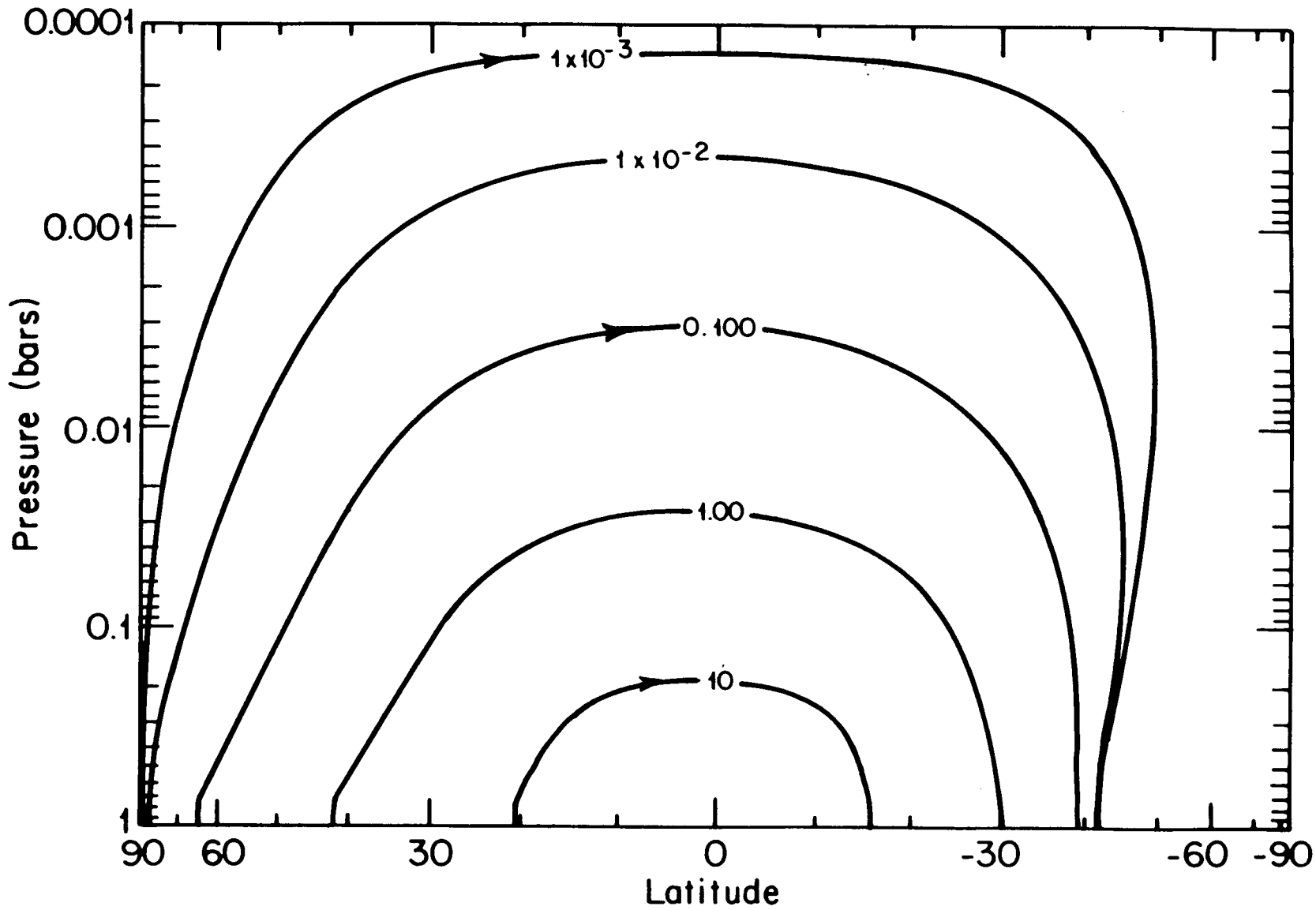
0.0001
0.001
0.01
0.1
1
Pressure (bars)
1x10-3
1 x 10-2
0.100
1.00
10
90
60
30
0
-30
-60
-90
Latitude

FIGURE 6

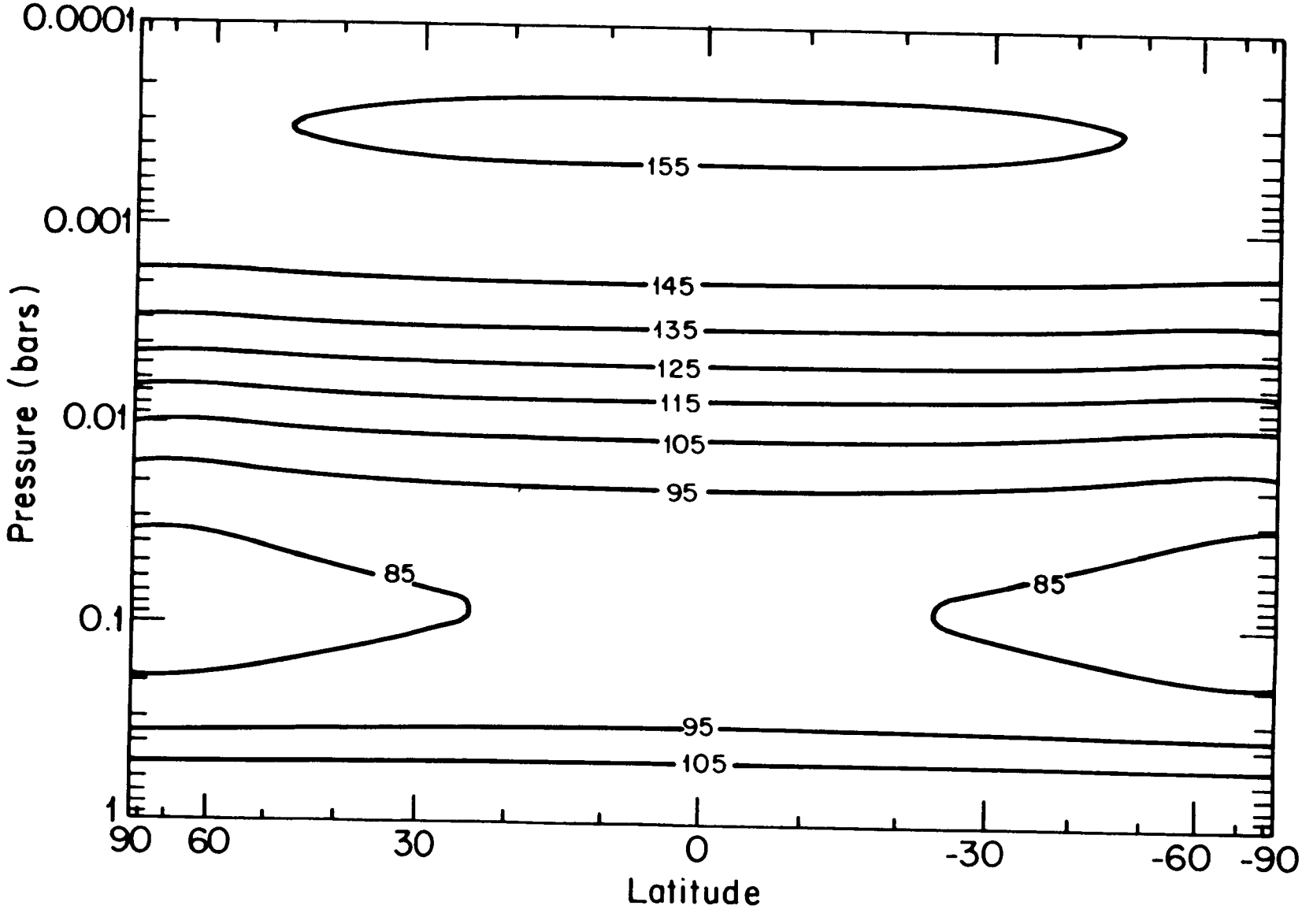
0.0001
0.001
0.01
0.1
1
Pressure (bars)
155
145
135
125
115
105
95
85
85
95
105
90
60
30
0
-30
-60
-90
Latitude

FIGURE 7

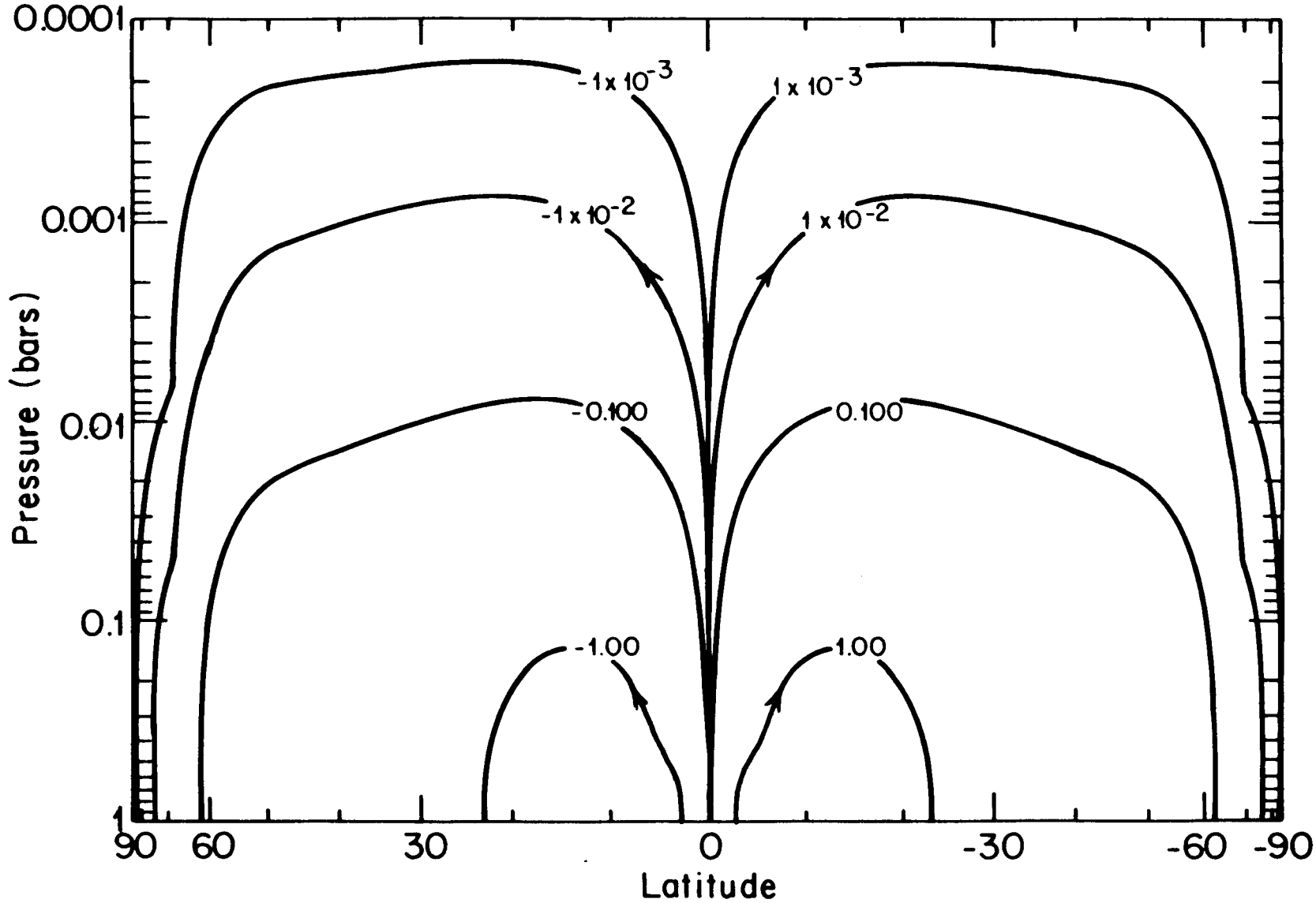
0.0001
0.001
0.01
0.1
1
Pressure (bars)
-1 x 10^-3
1 x 10^-3
-1 x 10^-2
1 x 10^-2
-0.100
0.100
-1.00
1.00
90
60
30
0
-30
-60
-90
Latitude

FIGURE 8a

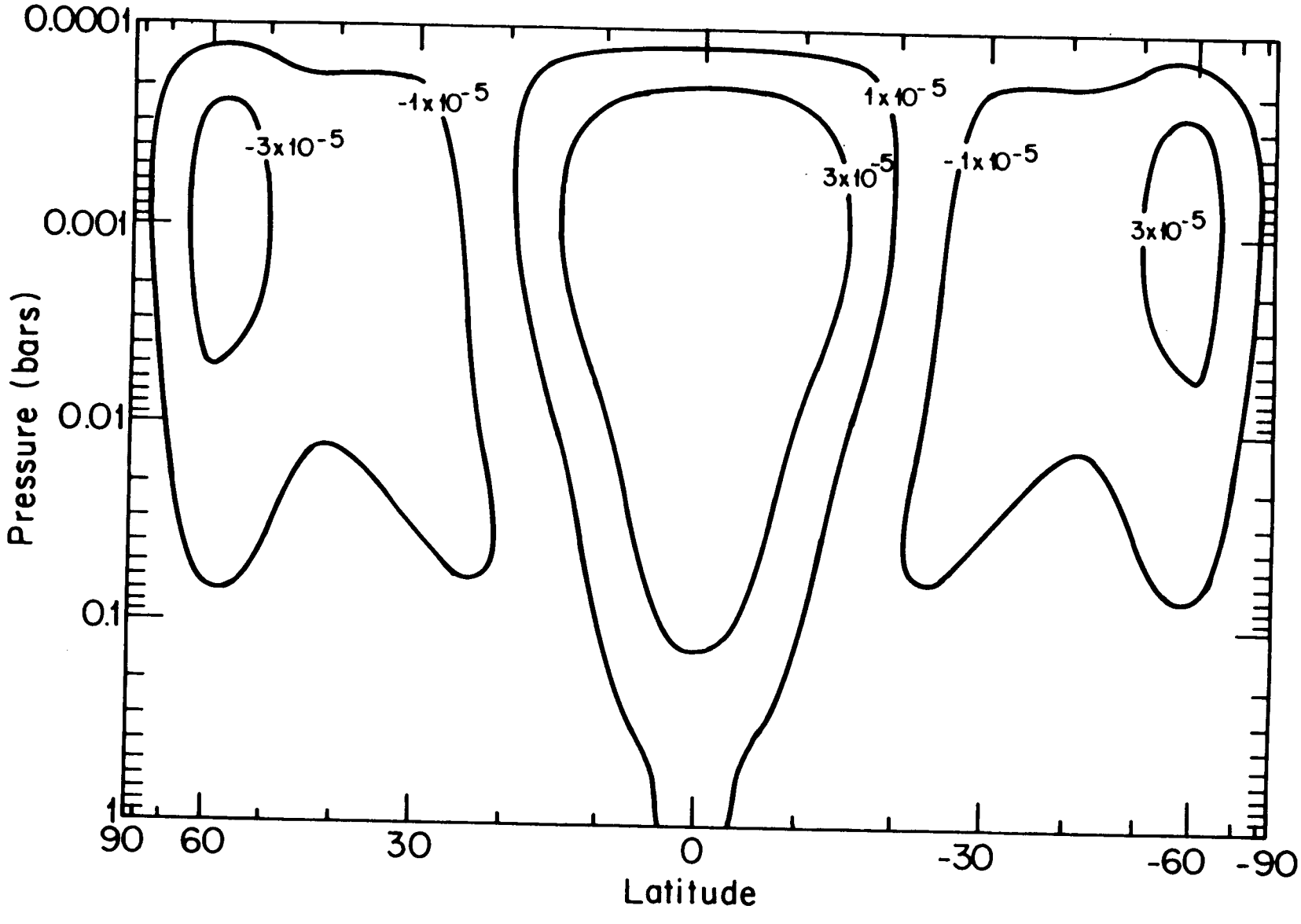
0.0001
0.001
0.01
0.1
1
Pressure (bars)
-1x10-5
-3x10-5
1x10-5
3x10-5
-1x10-5
3x10-5
90
60
30
0
-30
-60
-90
Latitude

FIGURE 8b

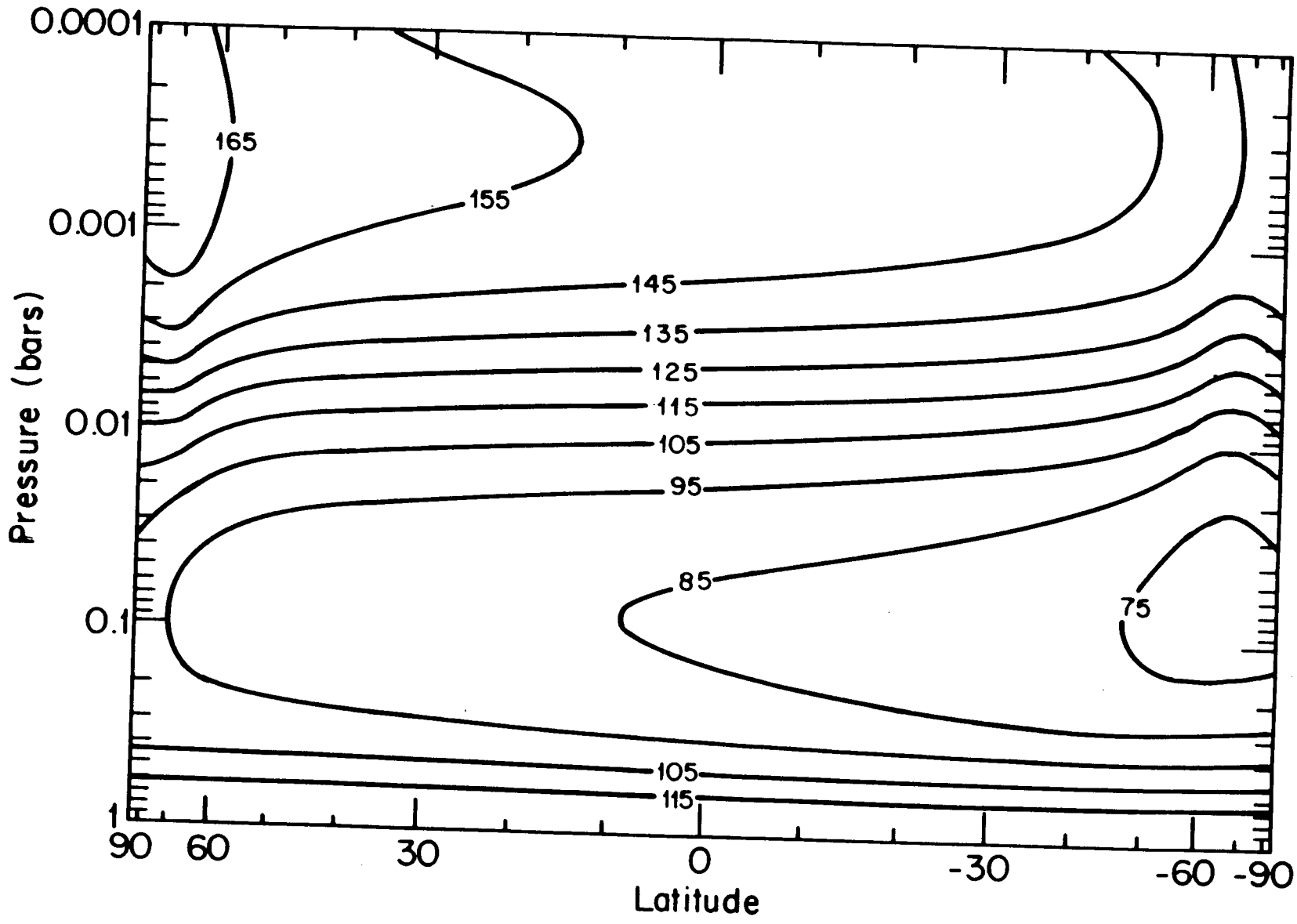
0.0001
0.001
0.01
0.1
1
Pressure (bars)
165
155
145
135
125
115
105
95
85
75
105
115
90
60
30
0
-30
-60
-90
Latitude

FIGURE 9a

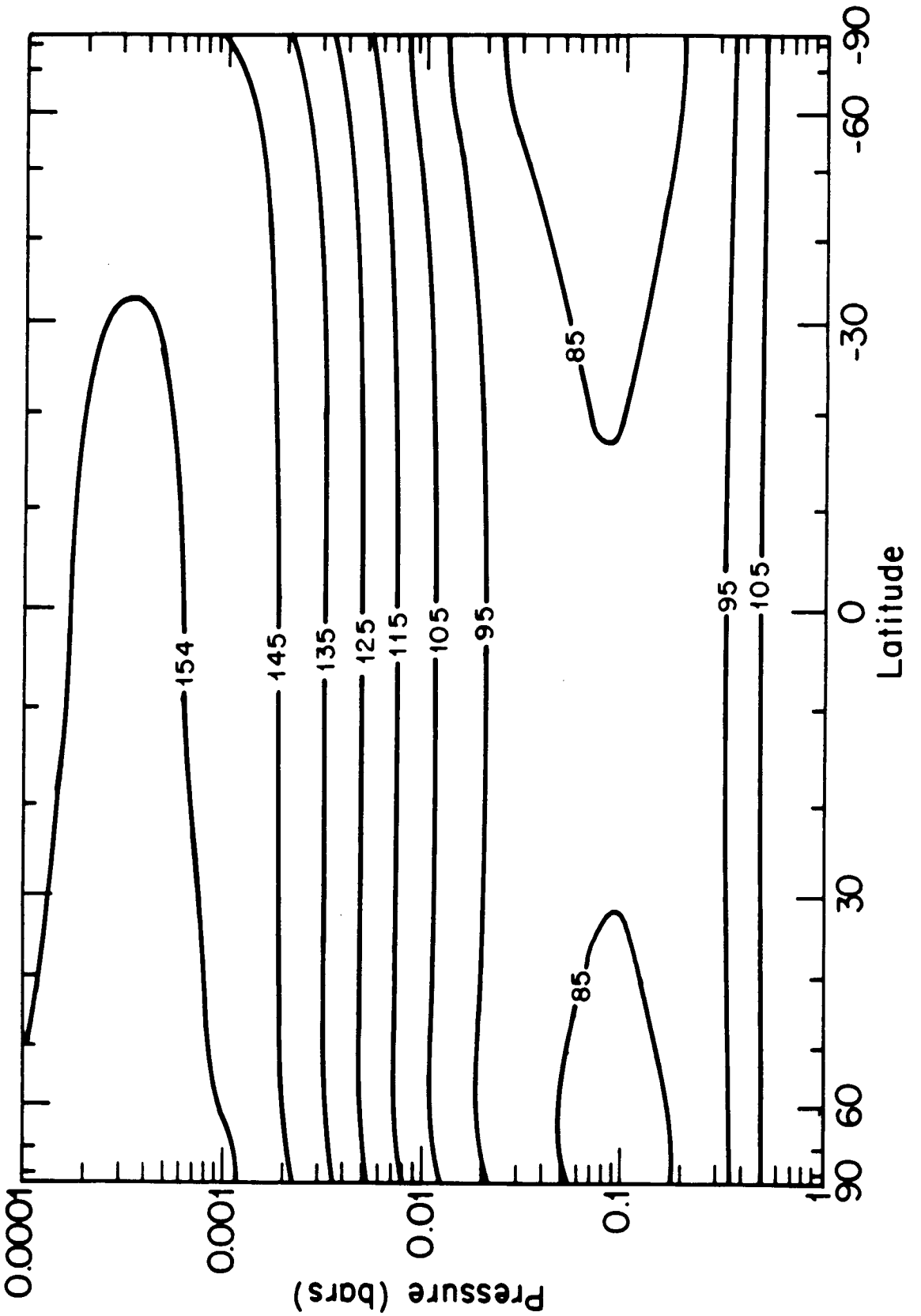
0.0001
0.001
0.01
0.1
1
Pressure (bars)
90
60
30
0
-30
-60
-90
Latitude
154
145
135
125
115
105
95
85
85
95
105

FIGURE 9b

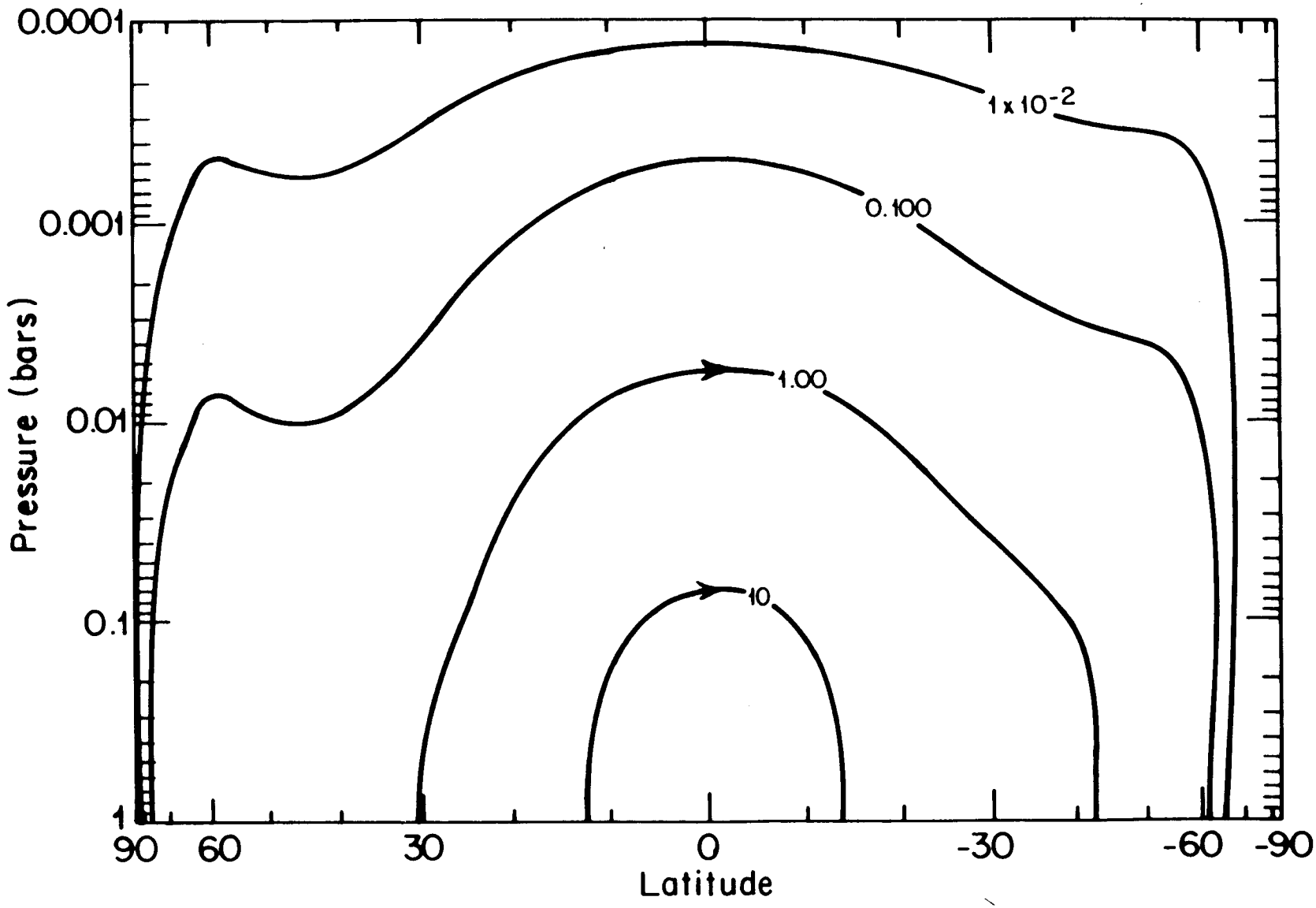
0.0001
0.001
0.01
0.1
1
Pressure (bars)
1 x 10-2
0.100
1.00
10
90
60
30
0
-30
-60
-90
Latitude

FIGURE 9c

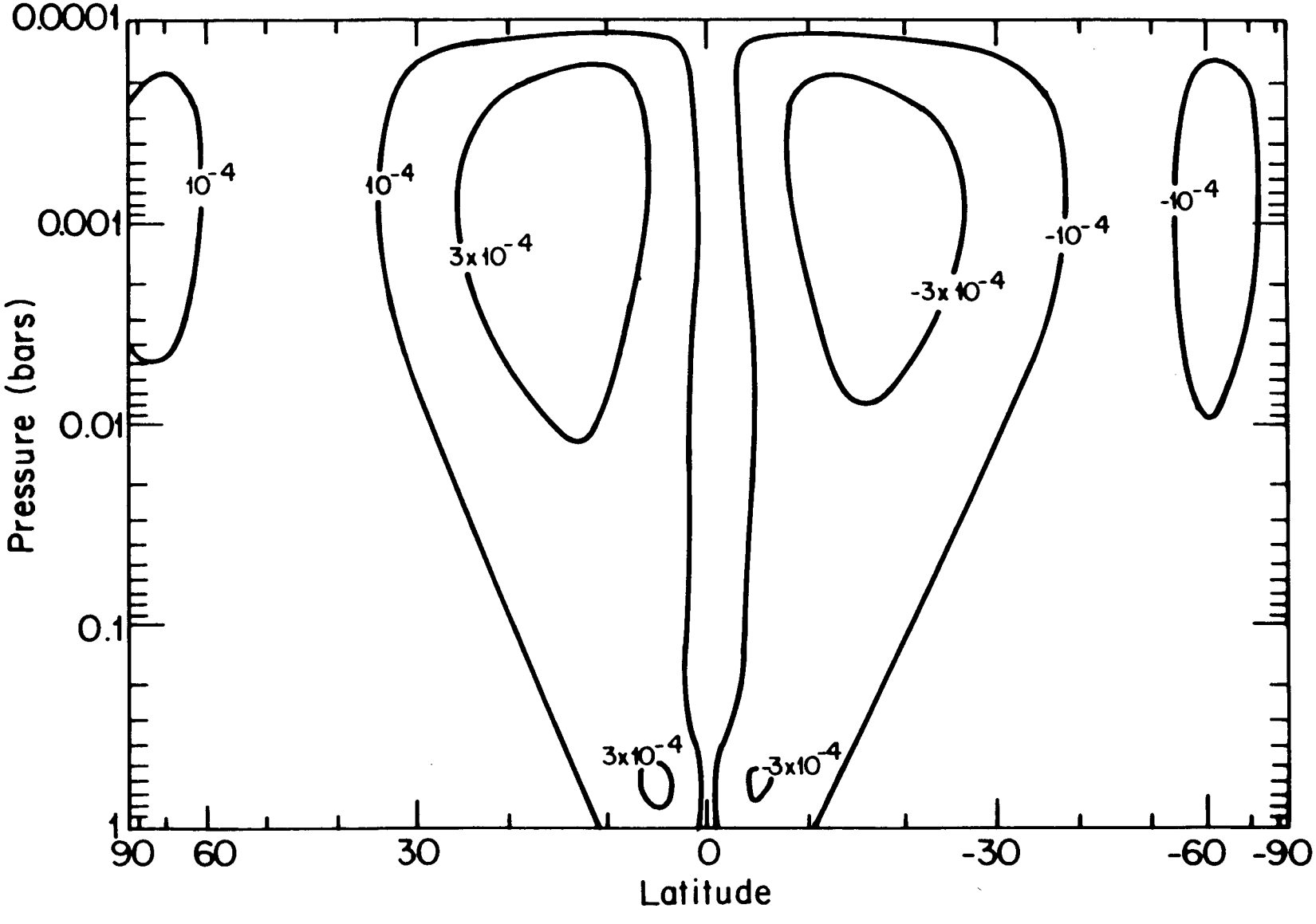
0.0001
0.001
0.01
0.1
1
Pressure (bars)
90
60
30
0
-30
-60
-90
Latitude
10^-4
10^-4
3x10^-4
-10^-4
-3x10^-4
-10^-4
3x10^-4
-3x10^-4

FIGURE 9d

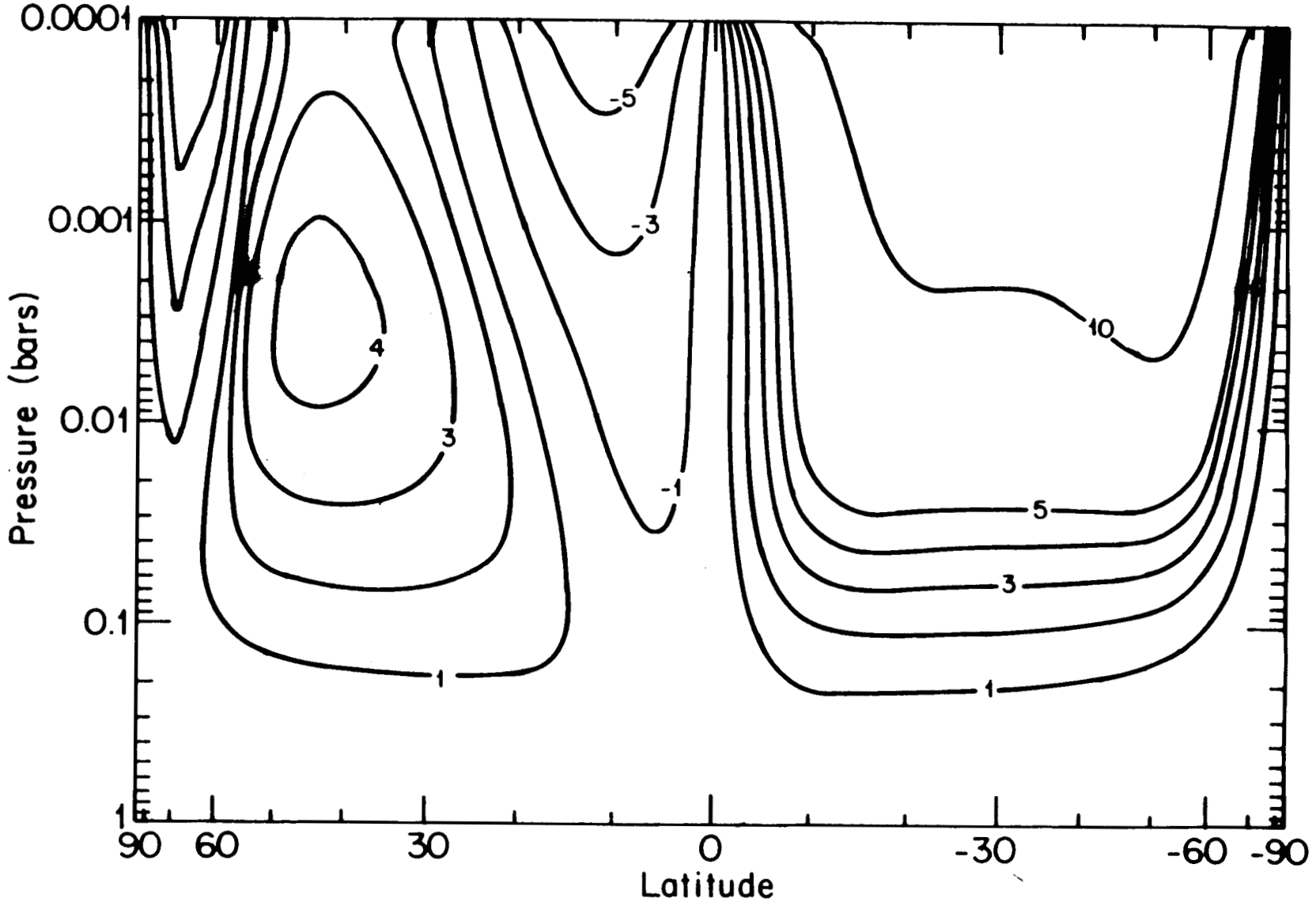
0.0001
0.001
0.01
0.1
1
Pressure (bars)
90
60
30
0
-30
-60
-90
Latitude
-5
-3
-1
4
3
1
10
5
3
1

FIGURE 9e

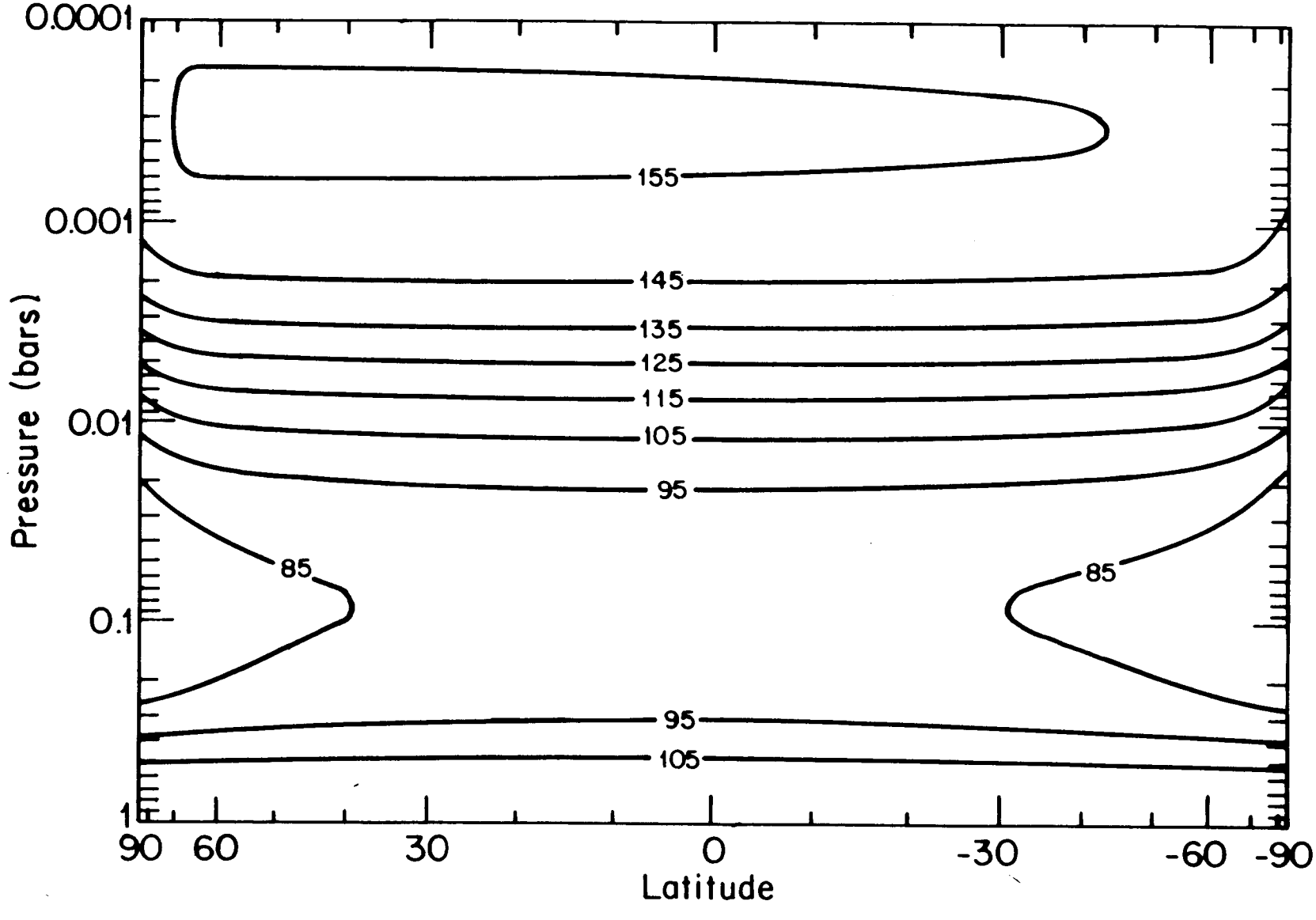
0.0001
0.001
0.01
0.1
1
Pressure (bars)
155
145
135
125
115
105
95
85
85
95
105
90
60
30
0
-30
-60
-90
Latitude

FIGURE 10a

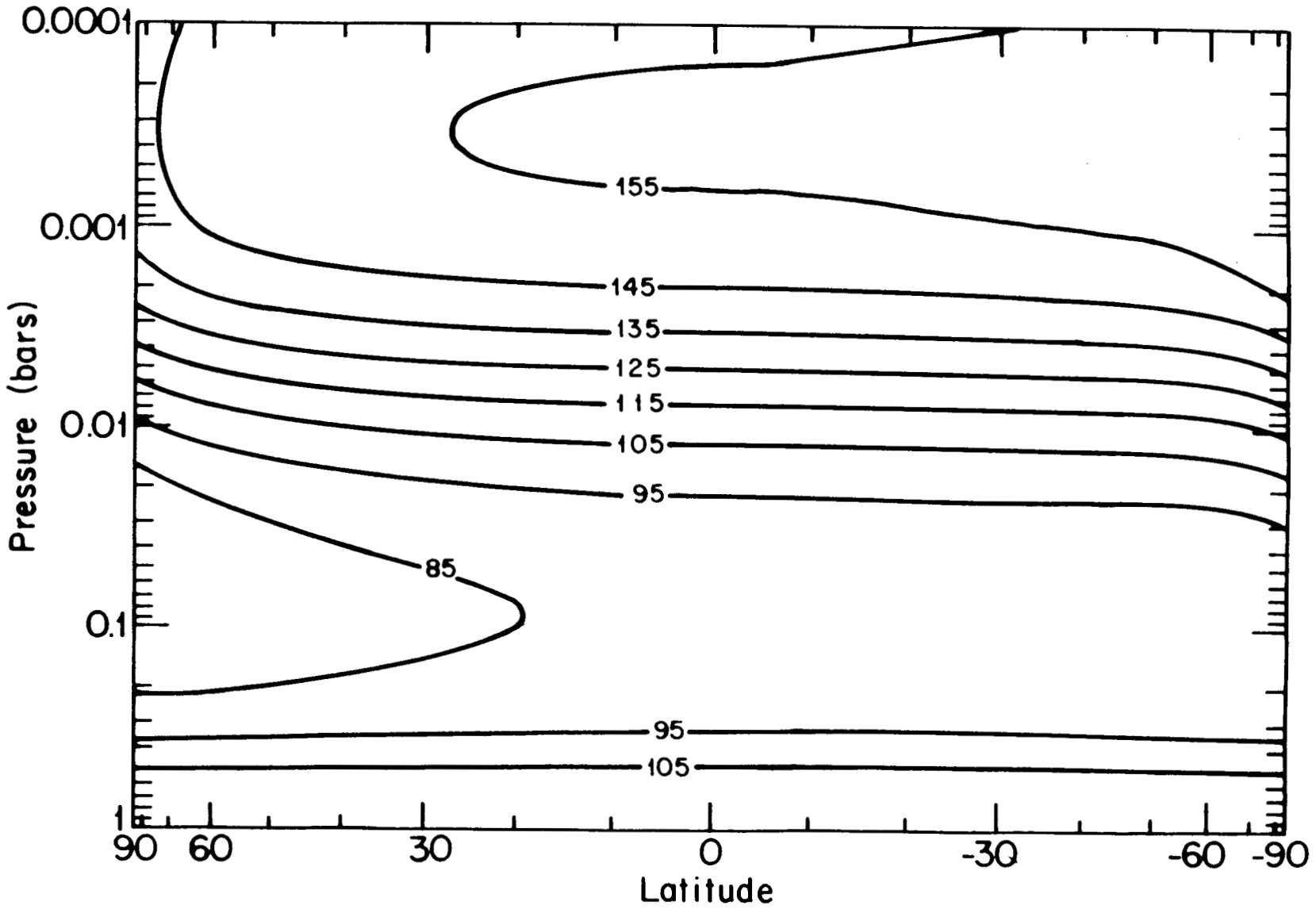
0.0001
0.001
0.01
0.1
1
Pressure (bars)
155
145
135
125
115
105
95
85
95
105
90
60
30
0
-30
-60
-90
Latitude

FIGURE 10b

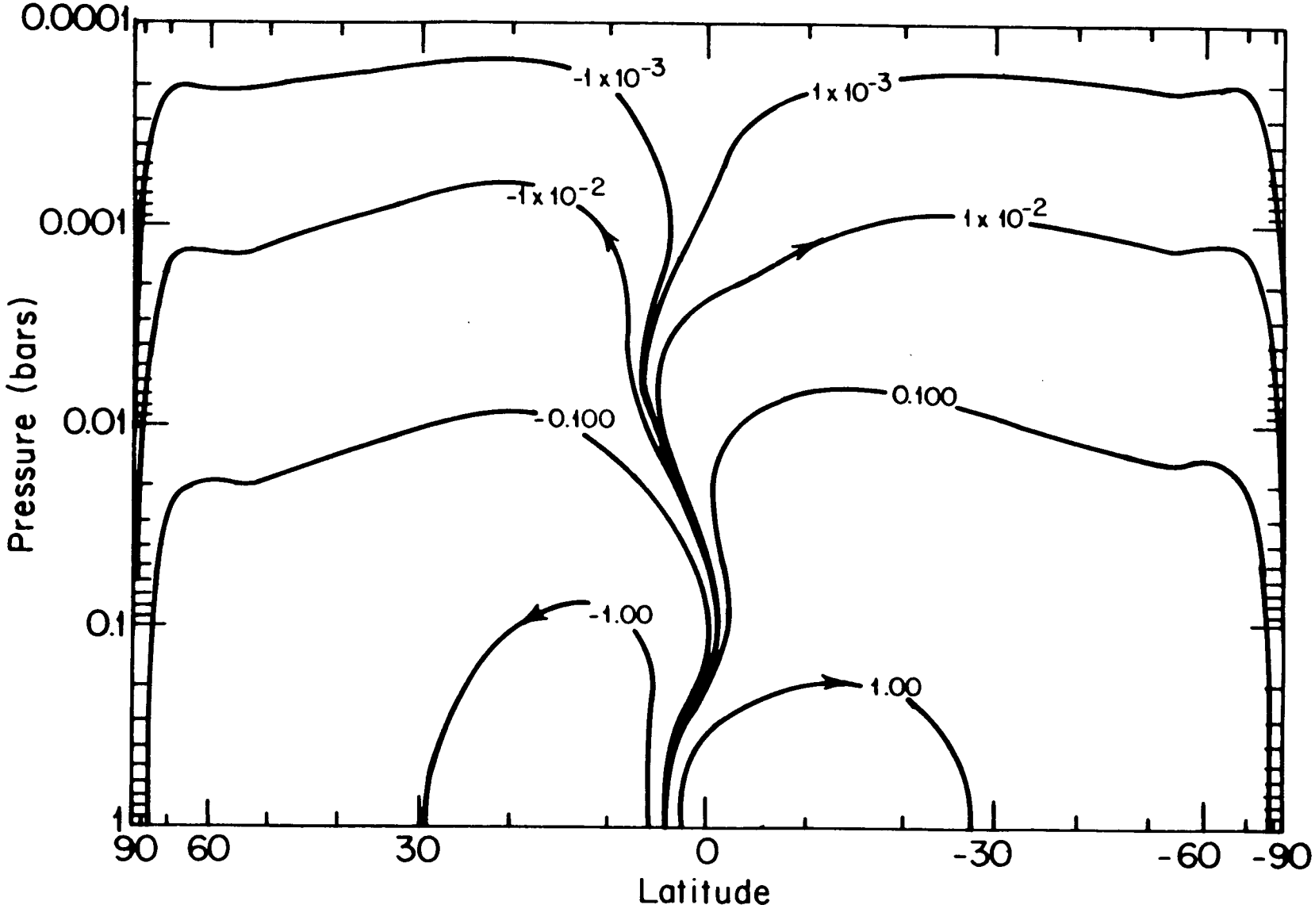
0.0001
0.001
0.01
0.1
1
Pressure (bars)
-1 x 10^-3
1 x 10^-3
-1 x 10^-2
1 x 10^-2
-0.100
0.100
-1.00
1.00
90
60
30
0
-30
-60
-90
Latitude

FIGURE 10c

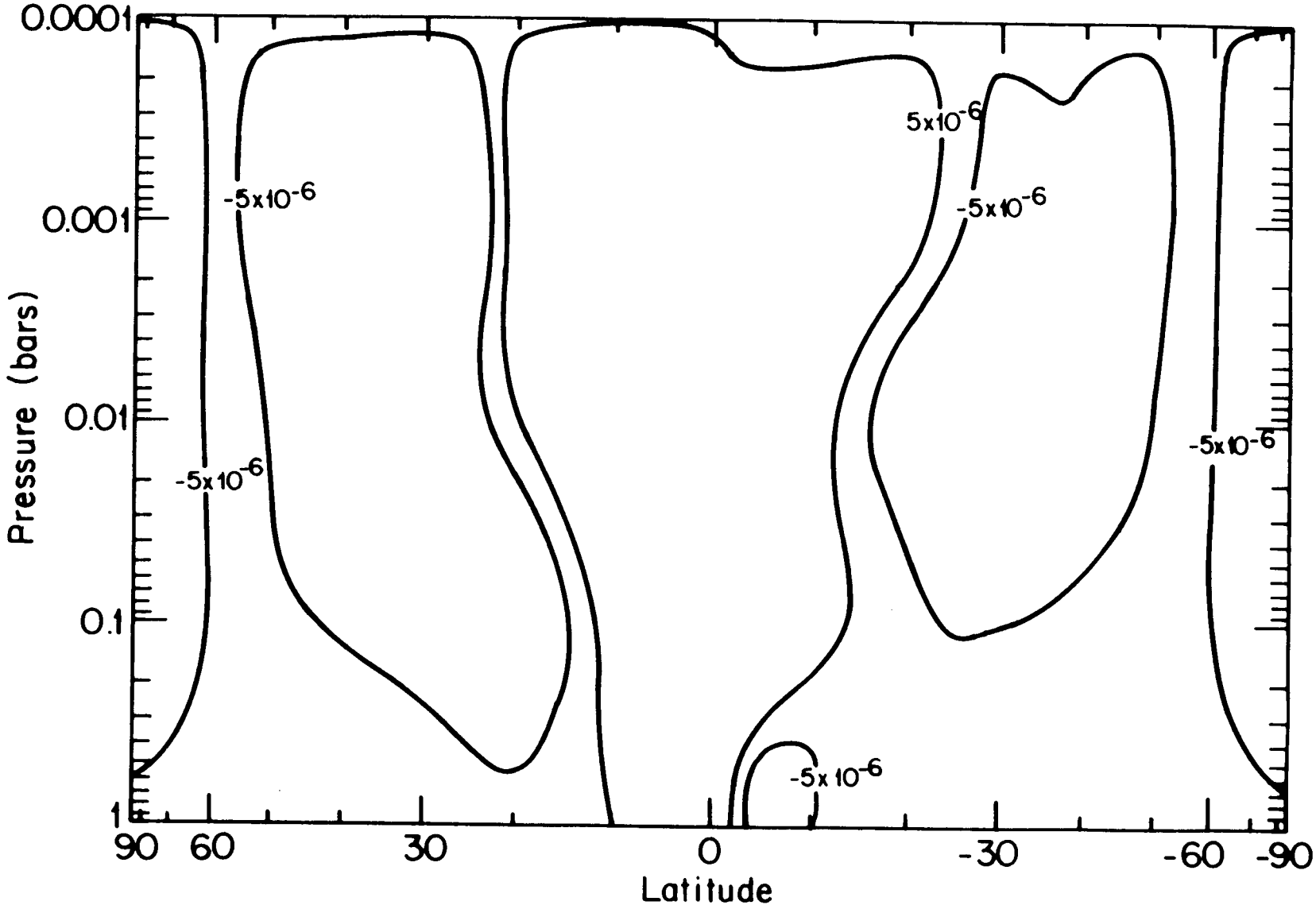
0.0001
0.001
0.01
0.1
1
Pressure (bars)
-5x10-6
-5x10-6
5x10-6
-5x10-6
-5x10-6
-5x10-6
90
60
30
0
-30
-60
-90
Latitude

FIGURE 10d

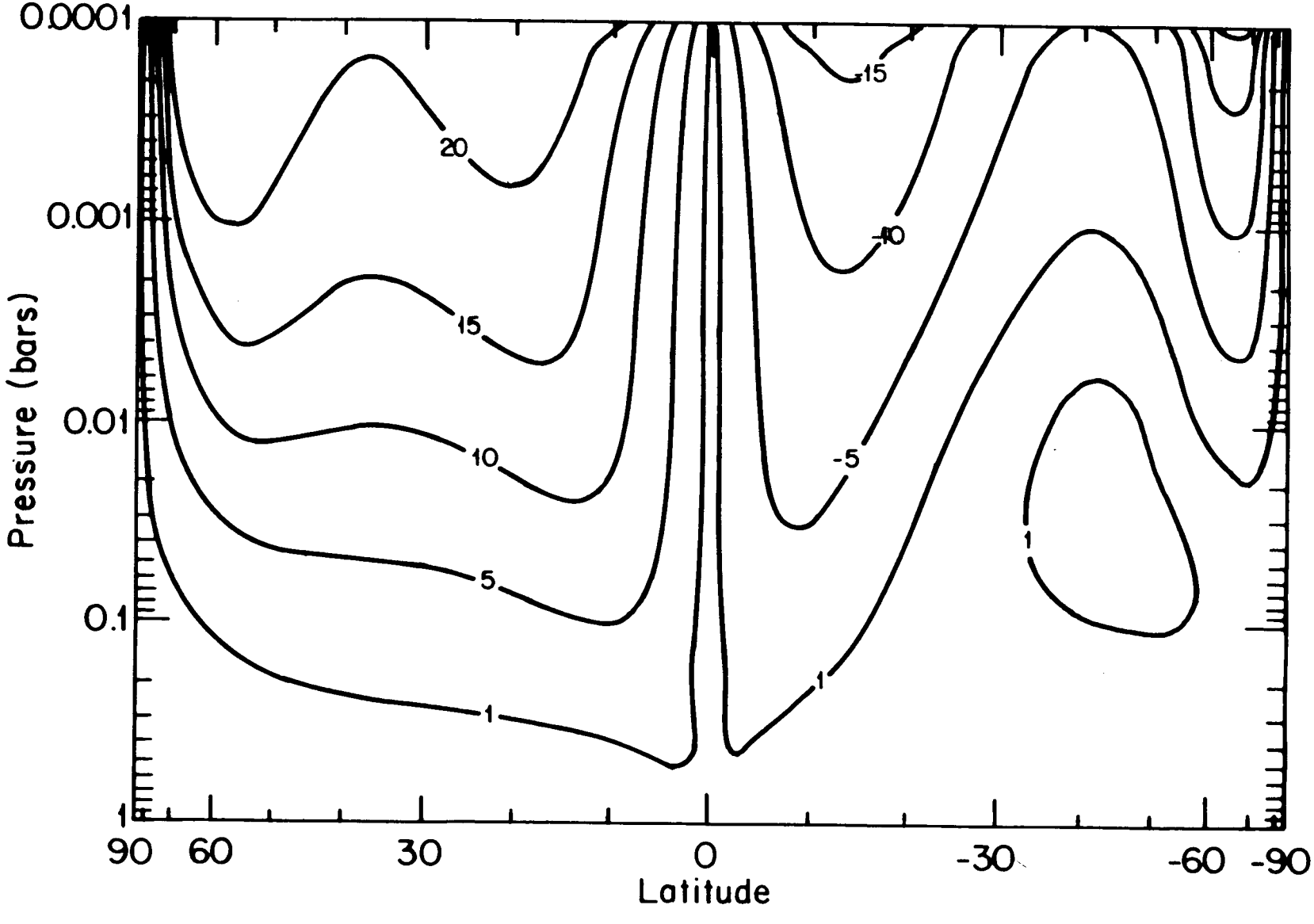
0.0001
0.001
0.01
0.1
1
Pressure (bars)
20
15
10
5
1
15
10
-5
1
90
60
30
0
-30
-60
-90
Latitude

FIGURE 10e

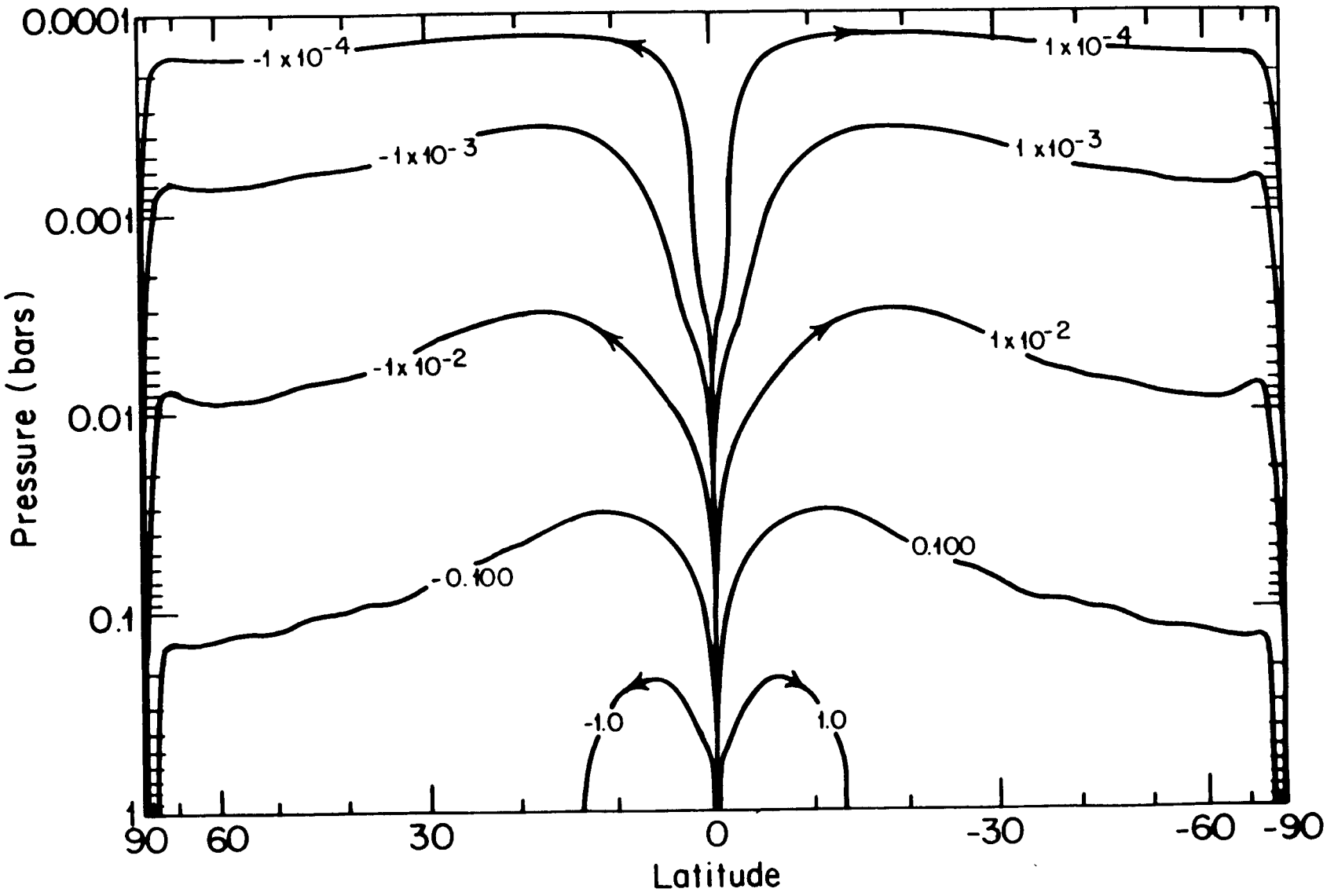
0.0001
0.001
0.01
0.1
1
Pressure (bars)
-1 x 10-4
1 x 10-4
-1 x 10-3
1 x 10-3
-1 x 10-2
1 x 10-2
-0.100
0.100
-1.0
1.0
90
60
30
0
-30
-60
-90
Latitude

FIGURE 11

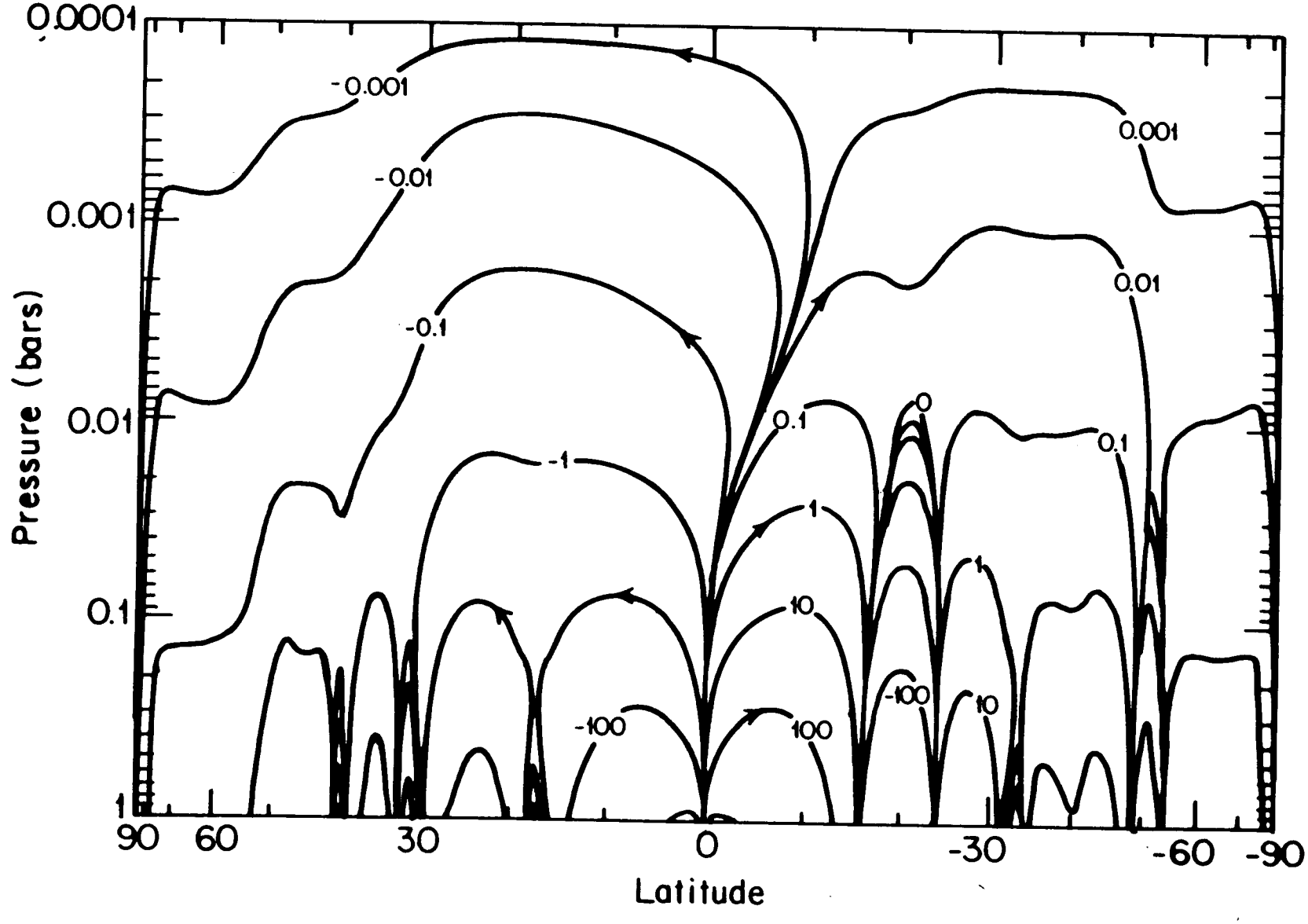
0.0001
0.001
0.01
0.1
1
Pressure (bars)
-0.001
-0.01
-0.1
-1
-100
100
0.001
0.01
0.1
0
1
10
-100
10
90
60
30
0
-30
-60
-90
Latitude

FIGURE 12a

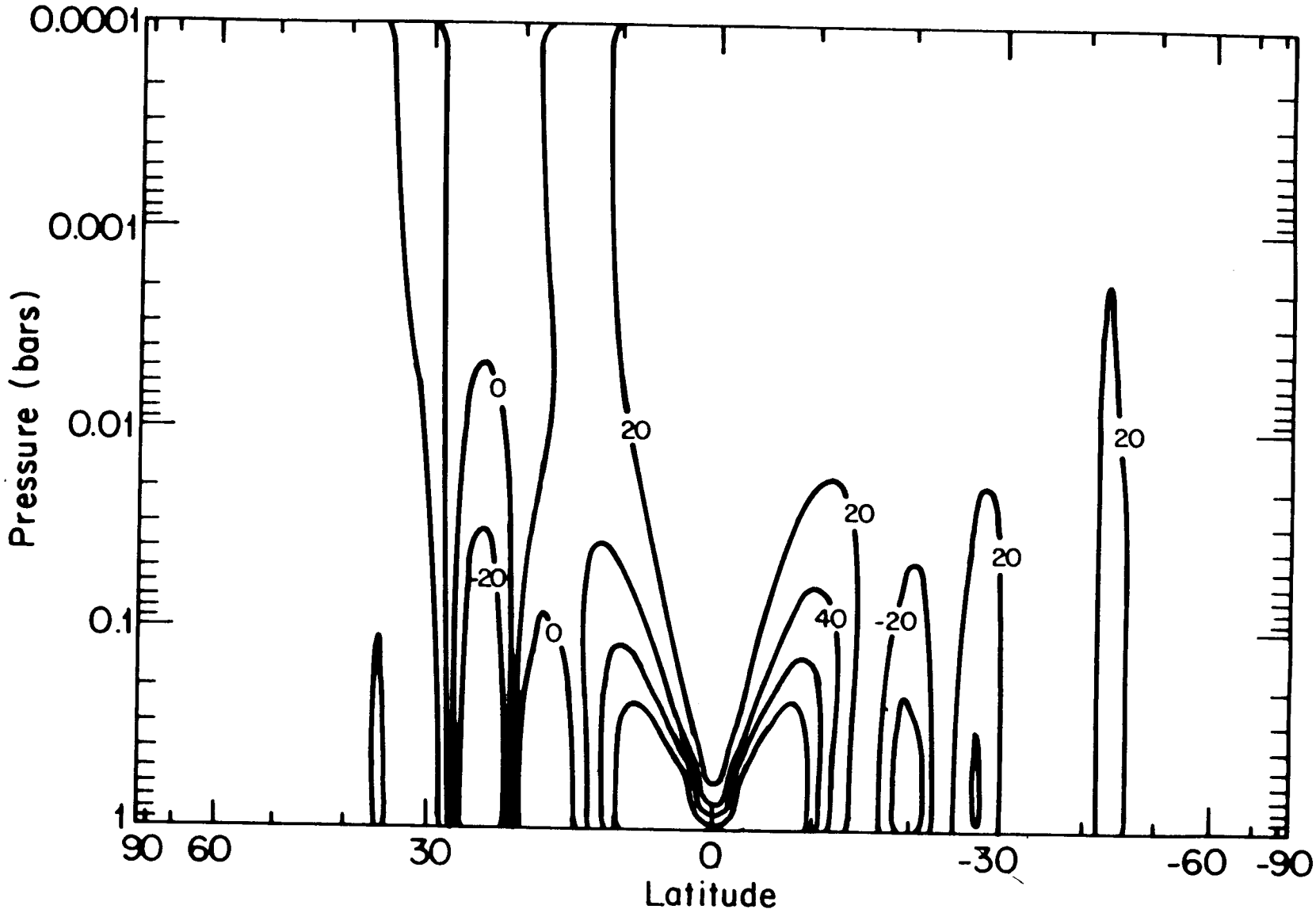
0.0001
0.001
0.01
0.1
1
Pressure (bars)
90
60
30
0
-30
-60
-90
Latitude
0
20
-20
0
20
20
40
-20
20
20

FIGURE 12b

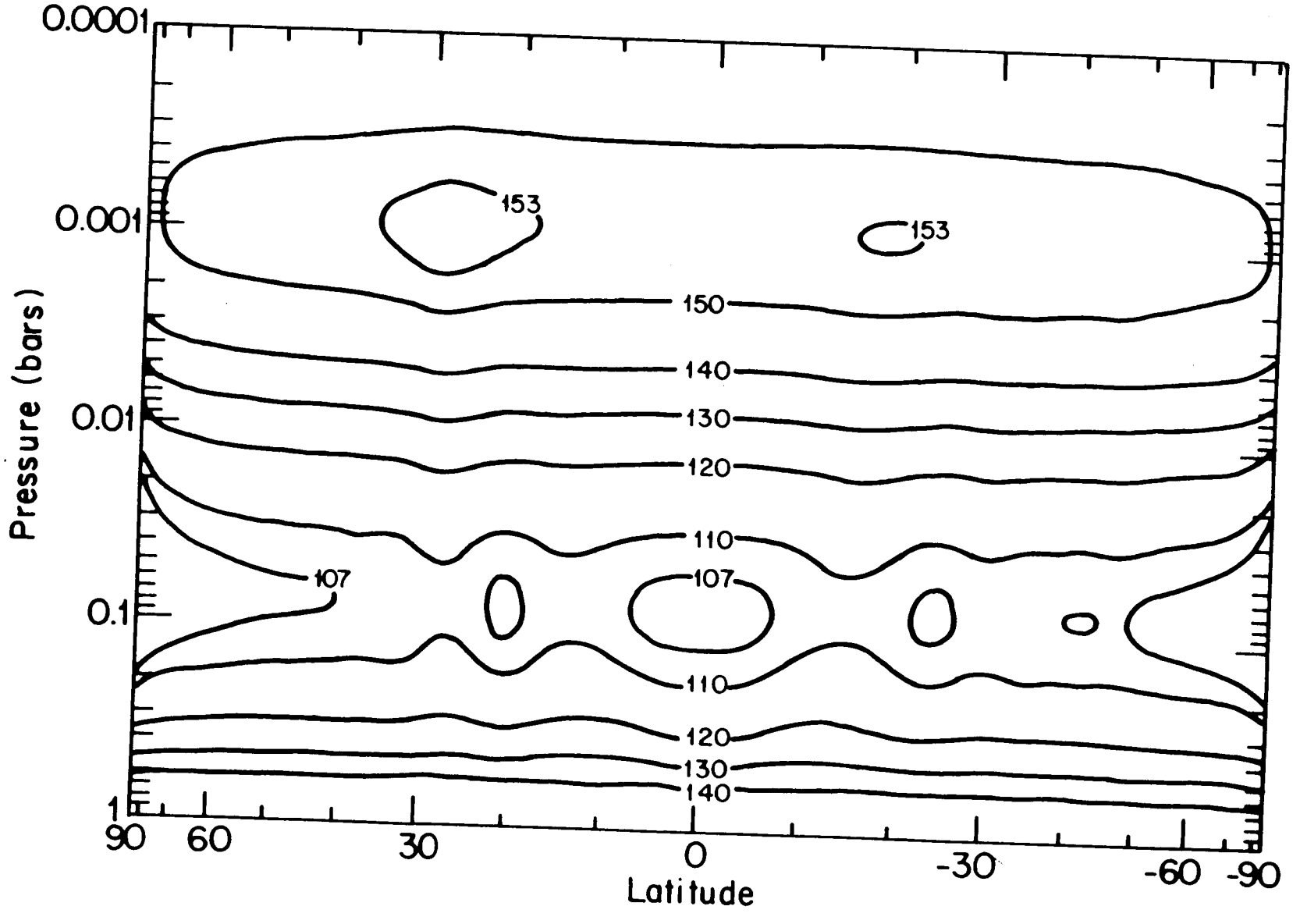
0.0001
0.001
0.01
0.1
1
Pressure (bars)
153
153
150
140
130
120
110
107
107
110
120
130
140
90
60
30
0
-30
-60
-90
Latitude

FIGURE 12c

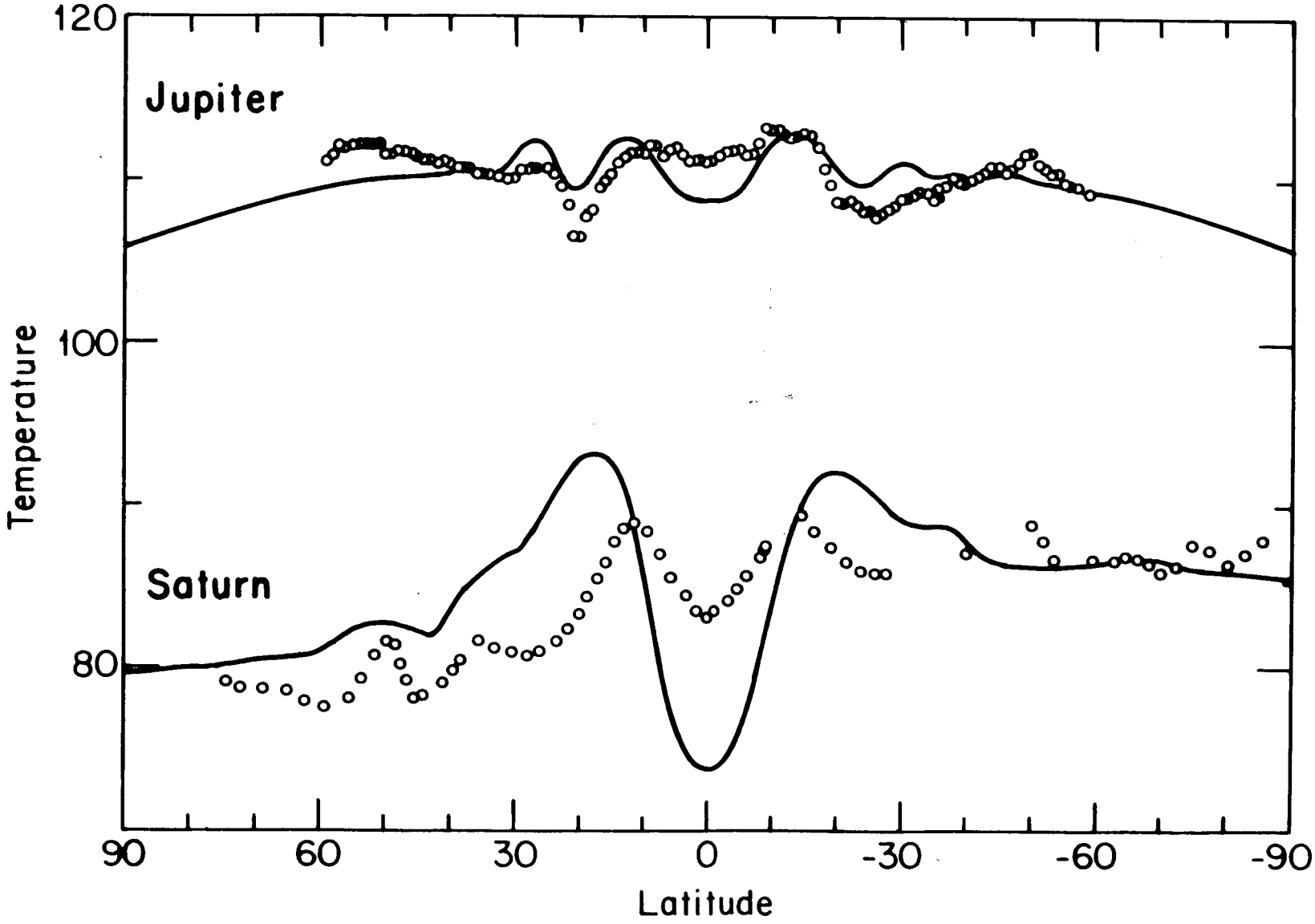
120
100
80
Temperature
Jupiter
Saturn
90
60
30
0
-30
-60
-90
Latitude

FIGURE 13